Society of Medical Education & Research

2025, Volume 5, Issue 2, Page No: 51-77
ISSN: 3108-4834

Archive of International Journal of Cancer and Allied Science

CST1 Suppresses Ferroptosis to Drive Gastric Cancer Metastasis via OTUB1-Mediated Stabilization of GPX4

Niels Henrik Rasmussen[1]*, Thomas Emil Sørensen[1]

[1]Department of Oncology, Odense University Hospital, Odense, Denmark.

***E-mail** ✉ n.rasmussen.ouh@outlook.com

Abstract

Metastasis is a key contributor to poor survival in gastric cancer patients, yet the underlying molecular mechanisms remain largely unclear. In this study, we investigated the potential role of cystatin SN (CST1), a cysteine protease inhibitor, in facilitating gastric cancer metastasis. We proposed that CST1 might drive cancer progression by influencing GPX4 and regulating ferroptosis. Transcriptome-wide analysis revealed that CST1 levels were markedly higher in metastatic tumors, and patients with elevated CST1 had poorer clinical outcomes. Functional experiments demonstrated that CST1 overexpression significantly enhanced the migratory and invasive abilities of gastric cancer cells in vitro and promoted metastasis to the liver, lungs, and peritoneum in mouse models. Additionally, high CST1 expression was associated with activation of the epithelial-mesenchymal transition (EMT) program. Mechanistically, CST1 was found to interact directly with GPX4, a central regulator of ferroptosis, as shown by co-immunoprecipitation and mass spectrometry. CST1 increased GPX4 protein stability by recruiting OTUB1, which reduced GPX4 ubiquitination, leading to decreased intracellular reactive oxygen species (ROS) levels and inhibition of ferroptosis. Through this mechanism, CST1 contributes to enhanced metastatic potential in gastric cancer cells. Clinically, CST1 levels were elevated in the peripheral blood and ascites of patients with metastatic disease, and multivariate Cox regression identified CST1 as an independent prognostic marker. In summary, our study uncovers a pathway whereby CST1 protects gastric cancer cells from ferroptotic cell death, thereby promoting tumor progression and metastasis. These findings highlight CST1 as a promising biomarker and therapeutic target for managing metastatic gastric cancer.

Keywords: Cancer metastasis, Gastric cancer, CST1, Ferroptotic

Introduction

Gastric cancer (GC) is a malignant tumor of the digestive system, ranking as the fifth most frequently diagnosed cancer and the fourth leading cause of cancer-related deaths worldwide [1]. Metastasis is a primary factor determining the poor prognosis of GC patients, yet the molecular mechanisms driving metastatic spread remain poorly defined. Chemotherapy has been the mainstay treatment for patients with metastatic gastric cancer for many years, but recent evidence indicates that its overall efficacy is limited and survival outcomes remain unsatisfactory [2]. Therefore, exploring novel therapeutic strategies for metastatic GC is an urgent clinical need.

In recent years, molecular targeted therapies have emerged as promising approaches for the treatment of various malignancies. Cystatins (CSTs) are a group of widely distributed proteins that inhibit cysteine proteases and can be classified into three main types [3]. Cystatin SN (CST1), encoded by the CST1 gene, is a secreted peptide of approximately 14 kDa belonging to the type 2 cysteine protease inhibitor family [4]. The cystatin domain, consisting of about 100 amino acids, interacts with the active site of cysteine proteases, blocking their proteolytic activity [5, 6]. CST1 is predominantly expressed in tissues such as the submandibular gland,

Access this article online https://smerpub.com/

Received: 11 April 2025; **Accepted:** 04 September 2025

How to cite this article: Rasmussen NH, Sørensen TE. CST1 Suppresses Ferroptosis to Drive Gastric Cancer Metastasis via OTUB1-Mediated Stabilization of GPX4. Arch Int J Cancer Allied Sci. 2025;5(2):51-77. https://doi.org/10.51847/NEuzwcD1pJ

gallbladder, and uterus, but it is also highly expressed in malignant tissues [7]. Recent studies have shown that CST1 overexpression contributes to tumor growth, invasion, and metastasis in cancers including lung, breast, and colorectal cancer [8-10]. For example, Kim et al. demonstrated that CST1 promotes colorectal tumorigenesis by counteracting the inhibition of CTSB proteolytic activity mediated by CST3 [11]. Furthermore, high CST1 levels were found to protect colorectal cancer cells from auranofin-induced cell death by suppressing intracellular reactive oxygen species (ROS) production [12]. In gastric cancer, CST1 has been reported to promote tumor progression through cathepsin inhibition and regulation of the transcription factor HOXC10 and the Wnt signaling pathway [13-15]. Despite these findings, the precise molecular mechanisms by which CST1 contributes to GC progression remain unclear.

Ferroptosis, a newly identified form of programmed cell death, is characterized by iron-dependent accumulation of lipid peroxides. Morphologically, cells undergoing ferroptosis exhibit increased ROS levels, reduced mitochondrial volume, and elevated membrane density [16, 17]. Emerging evidence suggests that ferroptosis plays an important role in tumor metastasis. For instance, lymphoid tissue can shield cancer cells from ferroptosis, thereby facilitating melanoma metastasis [18]. Additionally, inducing ferroptosis in a spontaneous HER2-positive breast cancer mouse model has been shown to suppress brain metastases [19].

Glutathione peroxidase 4 (GPX4) is a key regulator of ferroptosis and tumor behavior, functioning to maintain redox homeostasis by inhibiting lipid peroxidation and preventing cell death caused by oxidative membrane damage [20]. GPX4 is frequently upregulated in metastatic tumors and is closely associated with cancer progression [21, 22]. For example, Lu et al. reported that KLF2 suppresses renal cell carcinoma migration and invasion by modulating GPX4-dependent ferroptosis [23]. However, the contribution of GPX4-mediated ferroptosis to gastric cancer metastasis remains largely unexplored.

The ubiquitin-proteasome system (UPS) mediates the majority of protein degradation in eukaryotic cells, accounting for approximately 80–85% of total protein turnover. Key components of the UPS include ubiquitin molecules, substrate proteins, ubiquitin-conjugating enzyme (E1), ubiquitin-activating enzyme (E2), ubiquitin ligase (E3), deubiquitinases (DUBs), and the proteasome. Dysregulation of this system has been implicated in tumor development and metastasis [24, 25]. The UPS also modulates ferroptosis; for example, DMOCPTL, a parthenolide derivative, promotes GPX4 ubiquitination and degradation, enhancing ferroptotic cell death [26-28]. To date, only a few ubiquitin ligases and deubiquitinases targeting GPX4 have been identified.

In this study, we investigated the role of CST1 in promoting gastric cancer metastasis. We hypothesized that CST1 may drive GC progression by regulating GPX4 stability and ferroptosis.

Results and Discussion

CST1 is highly expressed in primary and metastatic gastric cancer and correlates with poor prognosis

To explore genes associated with peritoneal metastasis in gastric cancer (GC), we conducted RNA sequencing (RNA-seq) analysis comparing 4 pairs of primary GC tissues with their corresponding adjacent normal tissues. Only genes with a p-value <0.05 were considered significant. The RNA-seq analysis identified a total of 3,904 differentially expressed genes, and a heatmap was generated highlighting the 20 most upregulated and 20 most downregulated genes (**Figure 1a**). Among these genes, CST1 was notably upregulated in primary GC tissues. These findings were further confirmed by the volcano plot analysis, which showed a consistent pattern of CST1 overexpression (**Figure 1b**).

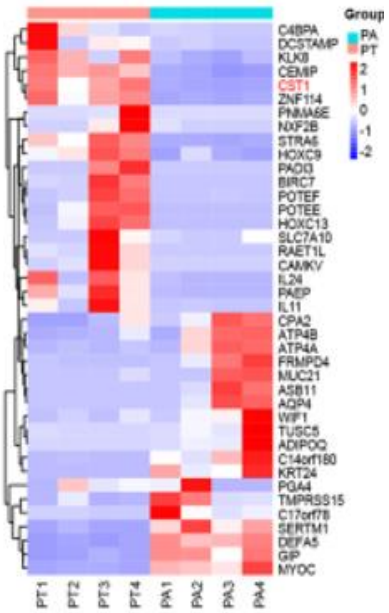
Group
PA
PT
C4BPA
DCSTAMP
KLK8
CEMIP
CST1
ZNF114
PNMA6E
NXF2B
STRA6
HOXC9
PADI3
BIRC7
POTEF
POTEE
HOXC13
SLC7A10
RAET1L
CAMKV
IL24
PAEP
IL11
CPA2
ATP4B
ATP4A
FRMPD4
MUC21
ASB11
AQP4
WIF1
TUSC5
ADIPOQ
C14orf180
KRT24
PGA4
TMPRSS15
C17orf78
SERTM1
DEFA5
GIP
MYOC
PT1
PT2
PT3
PT4
PA1
PA2
PA3
PA4

a)

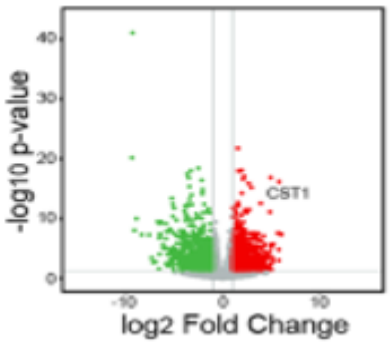
-log10 p-value
log2 Fold Change
CST1

b)

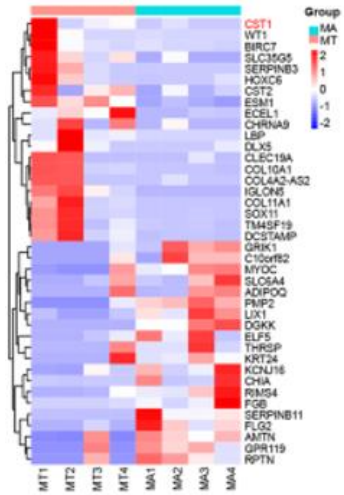
Group
MA
MT
CST1
WT1
BIRC7
SLC35G5
SERPINB3
HOXC6
CST2
ESM1
ECEL1
CHRNA9
LBP
DLX5
CLEC19A
COL10A1
COL4A2-AS2
IGLON5
COL11A1
SOX11
TM4SF19
DCSTAMP
GRIK1
C10orf82
MYOC
SLC5A4
ADIPOQ
PMP2
LIX1
DGKK
ELF5
THRSP
KRT24
KCNJ16
CHIA
RIMS4
PGB
SERPINB11
FLG2
AMTN
GPR119
RPTN
MT1
MT2
MT3
MT4
MA1
MA2
MA3
MA4

c)

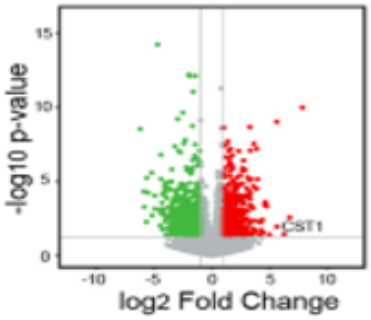
-log10 p-value
log2 Fold Change
CST1

d)

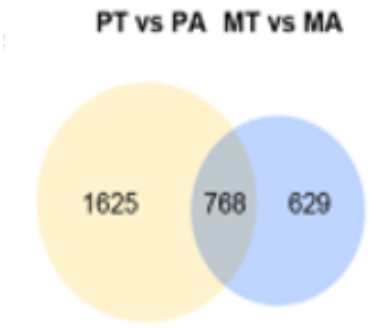
PT vs PA
MT vs MA
1625
768
629

e)

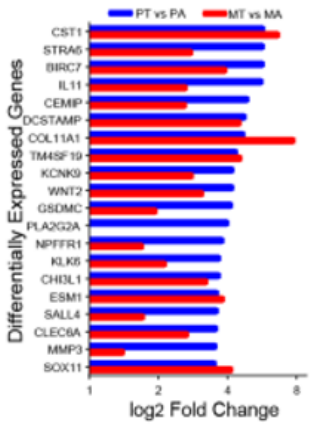
PT vs PA
MT vs MA
CST1
STRA6
BIRC7
IL11
CEMIP
DCSTAMP
COL11A1
TM4SF19
KCNK9
WNT2
GSDMC
PLA2G2A
NPFFR1
KLK6
CHI3L1
ESM1
SALL4
CLEC6A
MMP3
SOX11
Differentially Expressed Genes
log2 Fold Change

f)

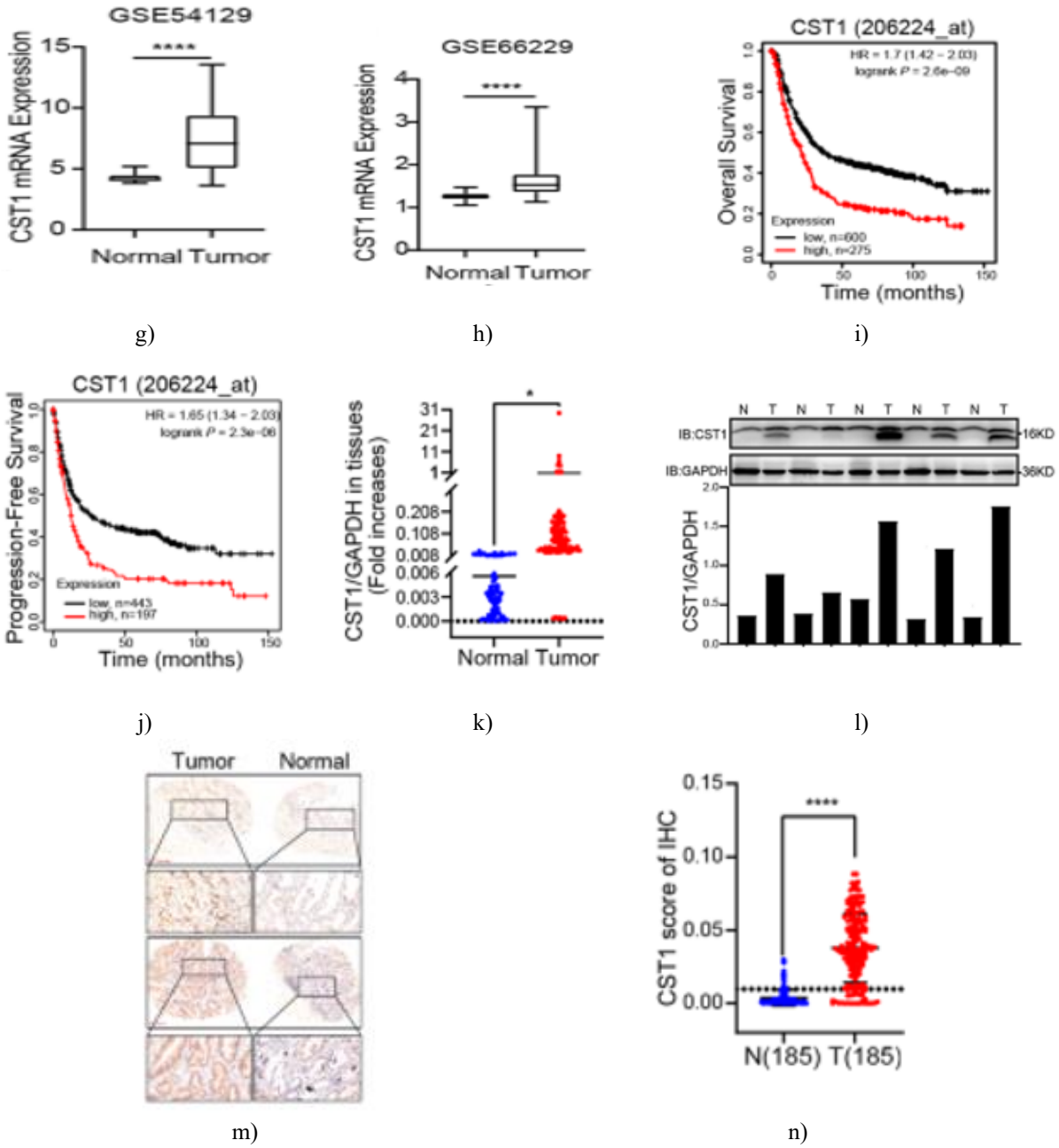

Figure 1. CST1 expression is elevated in both primary and metastatic GC tissues and is associated with poor prognosis**.**

Heatmaps depict the 20 most significantly upregulated and downregulated genes in primary GC **(a)** and metastatic GC **(c)** relative to adjacent normal tissues (>1.5-fold). Volcano plots illustrate the distribution of differentially expressed genes in primary GC **(b)** and metastatic GC **(d)**. A Venn diagram shows 768 genes upregulated in both conditions **(e),** and a histogram highlights the top 20 shared upregulated genes **(f)**. CST1 expression in GC versus matched normal tissues is shown in **(g, h)** based on GSE54129 and GSE66229. Kaplan–Meier survival curves for overall and progression-free survival are presented in **(i, j)** from the KM Plotter database. RT-qPCR of CST1 in 100 paired GC tissues is shown in **(k),** with data as mean ± SD of three independent experiments, analyzed by paired t-test (*p<0.05, n=100). Western blotting of CST1 in 5 paired GC samples is displayed in (L, upper panel), with quantification normalized to GAPDH (lower panel).

Representative IHC images of CST1 in GC tissues are shown in **(m),** scale bar 100 μm. IHC scoring of 185 GC and 185 normal tissues is presented in **(n),** statistical significance assessed by unpaired t-test (****p<0.0001). To further explore CST1 expression in GC metastasis, RNA-seq was performed on 4 paired peritoneal metastasized GC tissues. Heatmaps and volcano plots confirmed that CST1 expression was elevated in these metastatic samples (**Figures 1c and 1d**). Venn diagram analysis revealed 768 commonly upregulated genes between primary and metastatic clusters, including CST1 (**Figures 1e and 1f**).

Validation across independent datasets corroborated these findings. CST1 levels were higher in GC tissues compared with normal controls in GSE66229 and GSE54129 (**Figures 1g and 1h**), as well as GSE26899, GSE79973, GSE19826, GSE13911 (**Figure 1a**), and TCGA (**Figure 1b**). CST1 expression appeared to trend with clinical stage, although statistical significance was not reached (**Figure 1c**). Importantly, Kaplan–Meier analysis indicated that patients with higher CST1 levels experienced worse overall and progression-free survival (**Figures 1i and 1j**).

Experimental confirmation in clinical samples supported these observations. RT-qPCR of 100 paired GC and adjacent normal tissues demonstrated significantly higher CST1 mRNA in tumors (**Figure 1k**). Western blot analysis of 5 paired samples confirmed elevated CST1 protein levels in GC compared to normal tissues, with densitometry normalized to GAPDH (**Figure 1l**). IHC showed strong CST1 expression in tumors irrespective of differentiation status (**Figure 1m**), with poorly differentiated tissues in the upper panel and well-differentiated in the lower panel. IHC scoring of 185 paired samples reinforced that CST1 is significantly upregulated in GC tissues (**Figure 1n**).

CST1 enhances GC cell migration but does not affect proliferation in vitro

CST1 mRNA and protein levels were assessed across GC cell lines. AGS, BGC823, and MKN45 exhibited higher CST1 expression than HGC-27 and SNU-1 (**Figures 2a and b)**. HGC-27 cells were engineered to overexpress CST1, while AGS and MKN45 cells underwent knockdown (**Figures 2c and 2a**) to examine functional effects. Cell proliferation, assessed by CCK8 and colony formation assays, was not altered by either CST1 overexpression or knockdown (**Figures 2d, e and 2b, c).** In contrast, wound healing assays demonstrated that CST1 significantly promotes cell migration. HGC-27 cells overexpressing CST1 migrated faster than controls, whereas knockdown in MKN45-sh1, MKN45-sh2, and AGS cells resulted in reduced migration relative to control groups (**Figures 2f and 2d**).

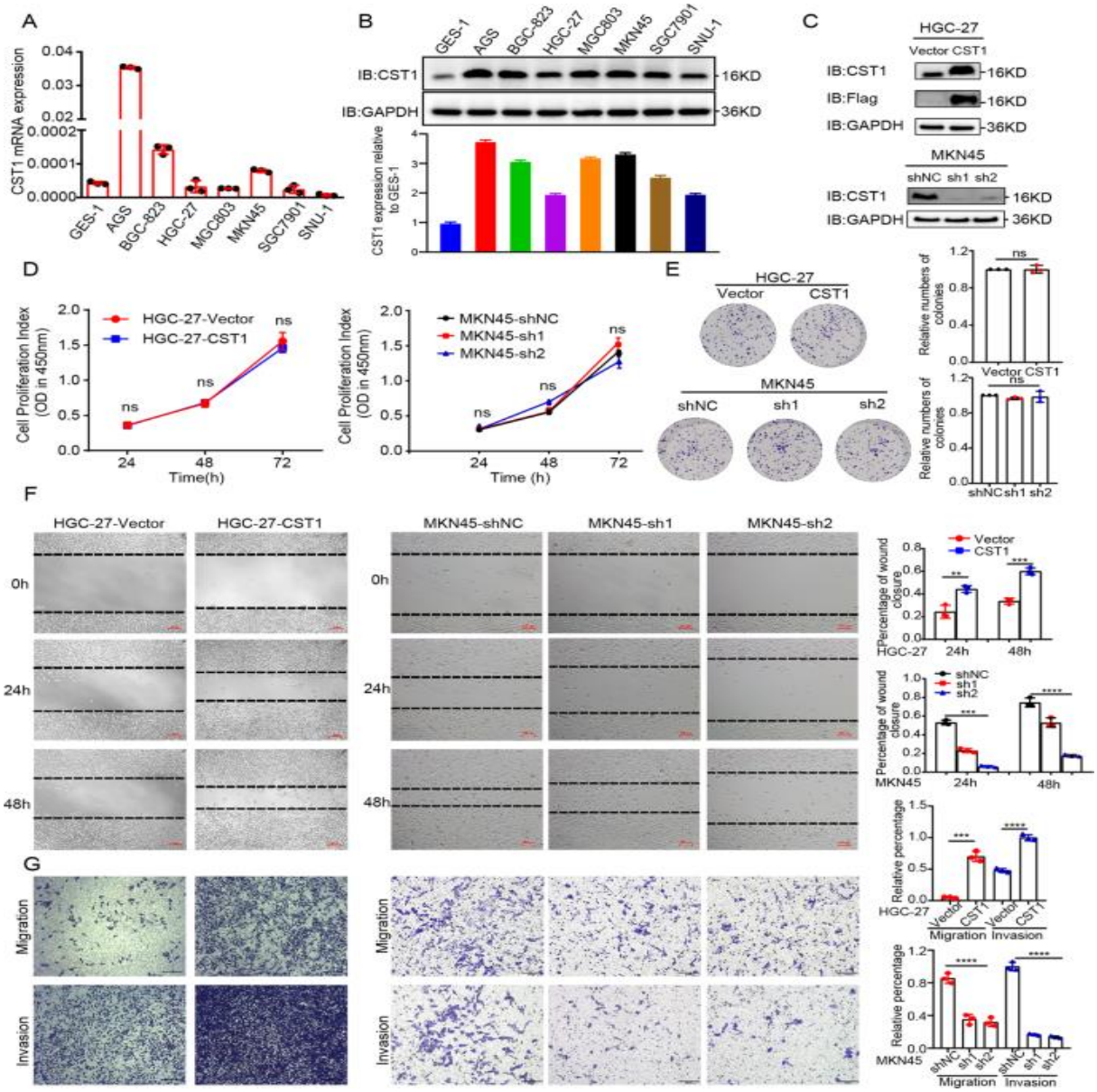

Figure 2. CST1 enhances metastasis of GC cells in vitro without affecting proliferation.

(A, B) CST1 expression levels were examined across different GC cell lines using RT-qPCR and Western blot, with total GAPDH as a loading control. **(C)** Stable overexpression of CST1 in HGC-27 cells and knockdown in MKN45 cells were verified by Western blot; GAPDH served as the loading control. **(D)** Proliferation was assessed using CCK8 assays in HGC-27-Vector/HGC-27-CST1 and MKN45-shNC/sh1/sh2-CST1 lines. Data are presented as mean ± SD from three independent experiments; paired t-test was applied for statistical analysis. **(E)** Colony formation assays were performed; representative images are shown on the left and quantification on the right. Mean ± SD from independent experiments are presented; unpaired t-test was used, ns indicates no significant difference. **(F)** Wound healing assays monitored cell migration at 0, 24, and 48 hours in HGC-27-Vector/HGC-27-CST1 and MKN45-shNC/sh1/sh2-CST1 cells. Representative images are shown on the left, with quantification on the right. Data are mean ± SD from independent experiments; unpaired t-test, ***$p < 0.001$. Scale bar: 100 μm. **(G)** Migration and invasion potential were evaluated using Transwell and Matrigel assays in CST1-overexpressing and CST1-knockdown stable lines. Left

panel shows representative images, right panel shows quantification. Data are mean ± SD; significance determined by unpaired t-test, ***p < 0.001. Scale bar: 100 μm.

To further investigate the functional role of CST1 in GC cell motility, migration and invasion assays were performed in HGC-27, AGS and MKN45 cells. Overexpression of CST1 significantly increased both migration and invasion in HGC-27 cells relative to control cells. Conversely, silencing CST1 in AGS and MKN45 cells led to a marked reduction in cell motility (**Figures 2g and 2e**). These results indicate that CST1 acts as a positive regulator of migratory and invasive phenotypes in GC cells.

CST1 interacts with GPX4 to maintain GPX4 protein stability

To explore the molecular mechanism of CST1 in GC, IP assays were performed in MKN45 cells using a CST1-specific antibody, with IgG as a negative control. Immunoprecipitated samples were separated by SDS-PAGE and subjected to LC-MS analysis; the experiment was repeated in triplicate (**Figure 3a**). Silver staining confirmed successful CST1 pull-down prior to LC-MS (**Figure 3b**). A Venn diagram identified 63 proteins enriched in CST1 IP compared with IgG controls. Proteins detected in all three independent mass spectrometry experiments were considered genuine interactors (**Figure 3c**). KEGG pathway enrichment analysis of these 63 proteins revealed a strong association with the ferroptosis pathway (**Figure 3d**), highlighting GPX4 as a key effector within this process.

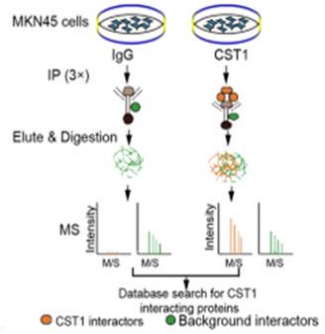

a)

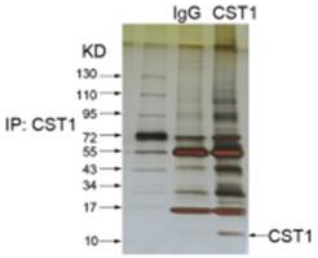

b)

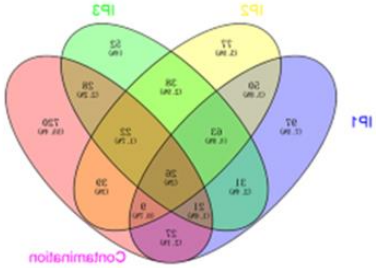

c)

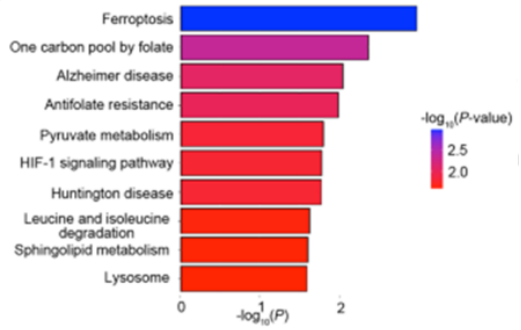

d)

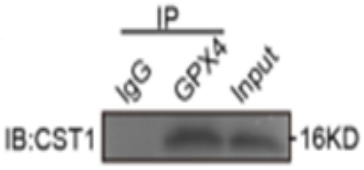

e)

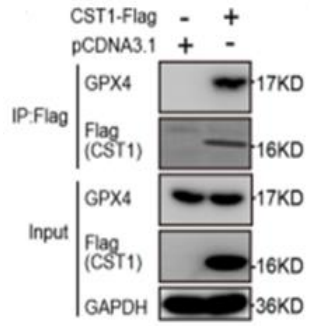

f)

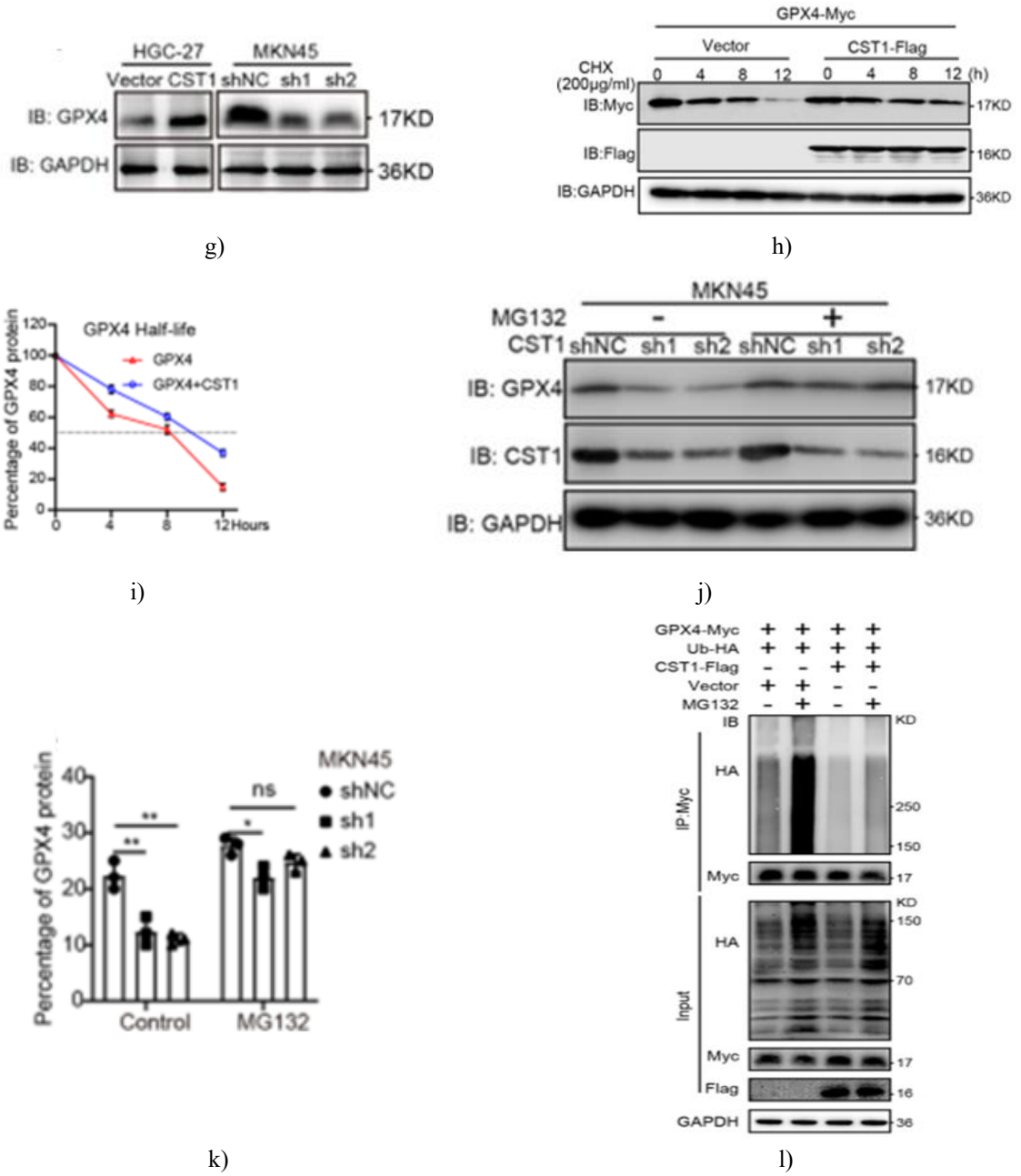

Figure 3. CST1 interacts with GPX4 to enhance GPX4 protein stability

(**a**) Schematic illustrating CST1 interactor identification. Proteins enriched in the CST1 experimental group compared with IgG controls were considered potential interactors. Three independent IP-MS experiments were conducted. (**b**) Silver staining of immunoprecipitated cell lysates. (**c**) Venn diagram showing 63 proteins consistently upregulated across three LC-MS replicates. (**d**) KEGG pathway enrichment analysis of the 63 shared proteins. (**e**) Co-immunoprecipitation (Co-IP) of CST1 using an anti-GPX4 antibody in MKN45 cells; IgG served as negative control. (**F**) Co-IP of GPX4 with anti-Flag antibody in HEK293T cells transiently expressing pcDNA3.1-FLAG-CST1; pcDNA3.1-vector served as control. (**g**) Western blot of GPX4 in HGC-27 and MKN45 stable lines; GAPDH as loading control. (**h, i**) GPX4 degradation after 200 μg/ml CHX treatment at indicated times in HEK293T cells co-transfected with Flag-CST1 and Myc-GPX4. (**j, k**) Western blotting of

GPX4 after 20 μM MG132 treatment for 4 h in MKN45 stable cells, expressed as fold-change relative to control. (**l**) Ubiquitination analysis of GPX4 by IP with anti-Myc and immunoblot with anti-HA and anti-Myc in HEK293T cells with indicated constructs.

To validate the CST1–GPX4 interaction, Co-IP experiments were performed in MKN45 cells overexpressing CST1 (**e**), revealing strong binding between CST1 and GPX4. HEK293T cells transiently expressing Flag-tagged CST1 were also analyzed by Co-IP, confirming physical interaction (**f**). These results suggest that CST1 binding to GPX4 may contribute to GC malignancy.

Next, we examined whether CST1 affects GPX4 at the mRNA or protein level. HGC-27-Vector/HGC-27-CST1 and MKN45-shNC/sh1/sh2-CST1 stable lines were established. RT-qPCR and Western blot analyses showed that CST1 overexpression increased GPX4 protein levels (**g**) without changing GPX4 mRNA (**Figure 3a**). GEO datasets GSE54129 and GSE66229 showed no significant correlation between CST1 and GPX4 mRNA expression (all $p > 0.05$) (**Figures 3b and c**).

To determine if CST1 stabilizes GPX4 protein, HEK293T cells co-transfected with Flag-CST1 and Myc-GPX4 plasmids were treated with 200 μg/ml CHX to inhibit protein synthesis. Western blotting showed that CST1 overexpression slowed GPX4 degradation compared with controls (**h, i**). Treatment with MG132 (20 μM, 4 h) caused GPX4 accumulation in MKN45-shNC/sh1/sh2-CST1 cells, and CST1 knockdown did not further reduce GPX4 levels (**j, k**). These results indicate that CST1 enhances GPX4 stability via the proteasome pathway.

CST1 inhibits GPX4 ubiquitination via OTUB1

Ubiquitination assays in HEK293T cells expressing Myc-GPX4 and HA-Ub, with or without Flag-CST1 and/or MG132, revealed high GPX4 ubiquitination in the absence of CST1 (L, lane 2), which was strongly reduced when CST1 was present (L, lanes 3–4), even without MG132 (L, lane 3). In CST1-knockdown MKN45 cells (sh1/sh2), immunoprecipitated GPX4 showed increased ubiquitination compared with shNC controls (**Figure 3d**), suggesting that CST1 inhibits GPX4 ubiquitination in GC cells.

Finally, potential deubiquitinases or E3 ligases for GPX4 were explored. GSEA of pre-GC transcriptomes and GEO dataset GSE66229, stratified by CST1-high vs. CST1-low groups, revealed enrichment of deubiquitination-related genes in CST1-high samples (**Figure 4a**), indicating that CST1 participates in protein deubiquitination processes.

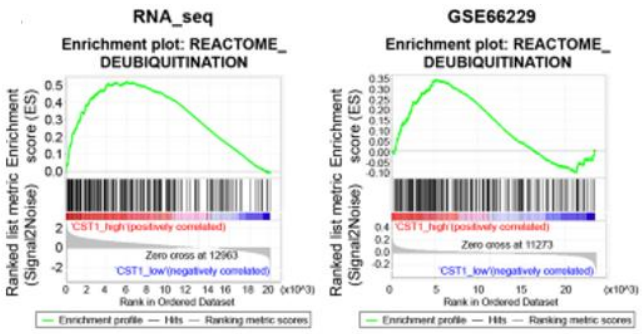

a)

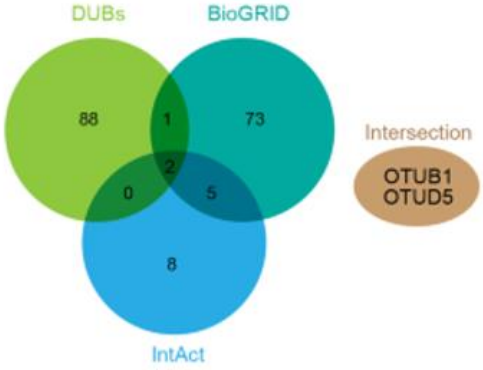

b)

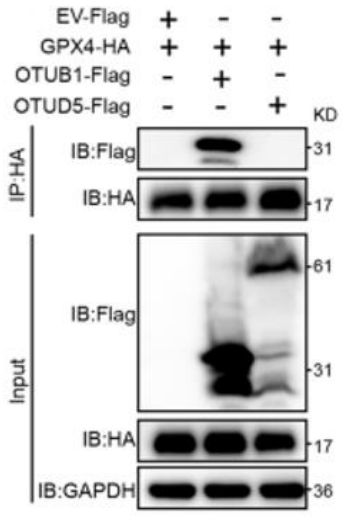
EV-Flag + - -
GPX4-HA + + +
OTUB1-Flag - + -
OTUD5-Flag - - +
KD
IP:HA
IB:Flag
IB:HA
31
17
Input
IB:Flag
IB:HA
IB:GAPDH
61
31
17
36

c)

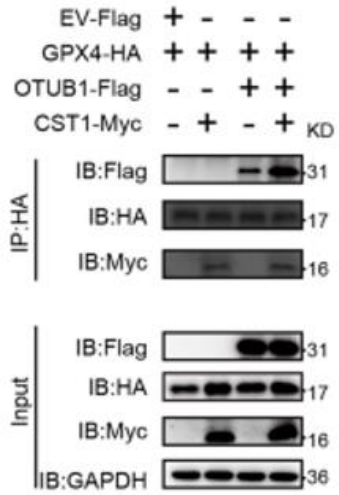
EV-Flag + - - -
GPX4-HA + + + +
OTUB1-Flag - - + +
CST1-Myc - + - +
KD
IP:HA
IB:Flag
IB:HA
IB:Myc
31
17
16
Input
IB:Flag
IB:HA
IB:Myc
IB:GAPDH
31
17
16
36

d)

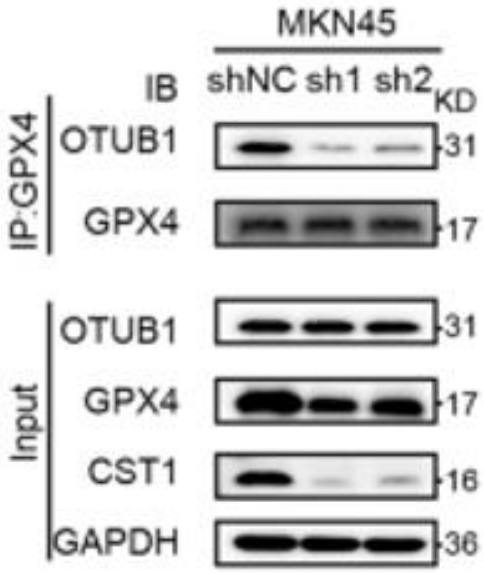
MKN45
IB
shNC sh1 sh2
KD
IP:GPX4
OTUB1
GPX4
31
17
Input
OTUB1
GPX4
CST1
GAPDH
31
17
16
36

e)

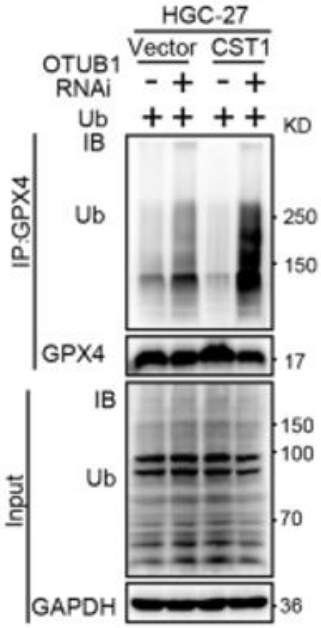
HGC-27
Vector CST1
OTUB1 RNAi - + - +
Ub + + + +
KD
IP:GPX4
IB
Ub
250
150
GPX4
17
Input
IB
Ub
150
100
70
GAPDH
36

f)

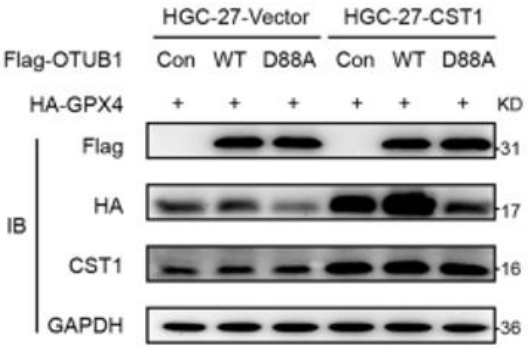
HGC-27-Vector
HGC-27-CST1
Flag-OTUB1 Con WT D88A Con WT D88A
HA-GPX4 + + + + + +
KD
IB
Flag
HA
CST1
GAPDH
31
17
16
36

g)

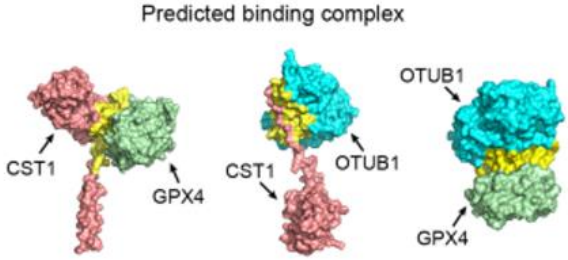
Predicted binding complex
CST1
GPX4
CST1
OTUB1
OTUB1
GPX4

h)

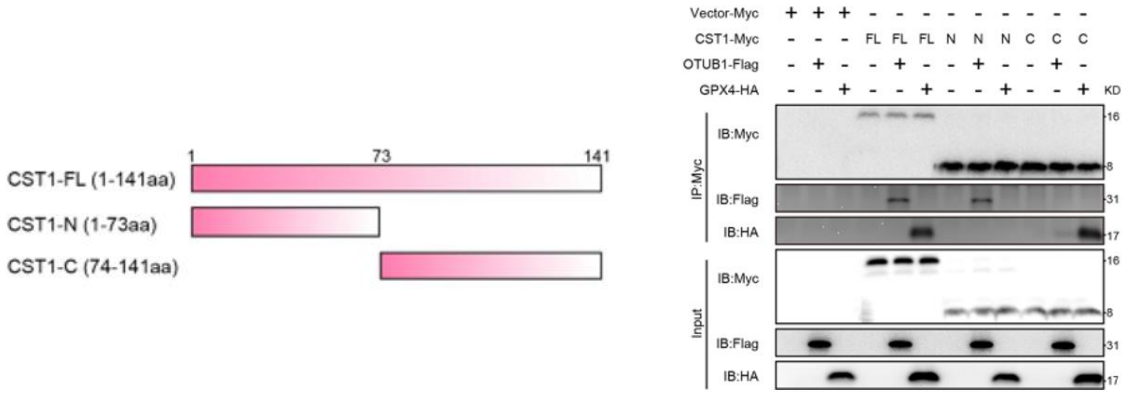

i) j)

Figure 4. CST1 alleviates GPX4 ubiquitination via the deubiquitinase OTUB1.

(**a**) GSEA of prior transcriptome sequencing and GEO dataset (GSE66229) revealed enrichment of genes involved in deubiquitination pathways. (**b**) Online databases (BioGRID, IntAct) were used to predict deubiquitinases (DUBs) that interact with GPX4; Venn analysis with all known DUBs identified OTUB1 and OTUD5 as potential interactors. (**c**) Co-IP in HEK293T cells transfected with Flag-tagged OTUB1 or OTUD5 plasmids to test binding with GPX4. (**d**) Western blot detection of Flag, HA, and Myc-tagged proteins after IP in cells co-transfected with Myc-CST1 and Flag-OTUB1. (**e**) Endogenous Co-IP in MKN45-shNC/sh1/sh2-CST1 cells; OTUB1 binding to GPX4 was reduced in CST1 knockdown lines. (**f**) HGC-27-Vector/HGC-27-CST1 cells transiently transfected with OTUB1 siRNA; ubiquitination assays showed increased GPX4 ubiquitin levels with OTUB1 reduction, amplified in CST1-overexpressing cells. (**g**) HGC-27-Vector/HGC-27-CST1 cells co-transfected with Flag-OTUB1-Con/WT/D88A and HA-GPX4; WB indicated that GPX4 stability was maintained in the OTUB1-WT group but reduced in OTUB1-D88A, especially with CST1 overexpression. (**h**) Predicted 3D binding model of CST1, OTUB1, and GPX4 using Cluspro. (**i**) Schematic of full-length and truncated CST1 constructs. (**J**) HEK293T cells transfected with CST1-FL/N/C-Myc along with OTUB1-Flag and GPX4-HA; Myc-IP showed CST1-FL and CST1-N bind OTUB1, while CST1-FL and CST1-C bind GPX4. SDS-PAGE for CST fragments was 15%. (Abbreviations: GSEA, Gene Set Enrichment Analysis; Con, control/empty plasmid; WT, wild-type; D88A, OTUB1 D88A point mutant).

By integrating database predictions and Venn analysis, OTUB1 and OTUD5 were identified as potential GPX4-interacting DUBs (**b**). Co-IP experiments in HEK293T cells revealed that only OTUB1 directly binds GPX4 (**c**). Co-transfection of Myc-CST1 and Flag-OTUB1 showed that CST1 enhances OTUB1 binding to GPX4 (**d**), while CST1 knockdown reduced OTUB1–GPX4 interaction (**e**). Transient OTUB1 silencing in HGC-27-Vector/CST1 cells increased GPX4 ubiquitination, particularly in CST1-overexpressing cells (**f**), indicating that CST1 facilitates GPX4 deubiquitination through OTUB1.

OTUB1's deubiquitinase activity relies on inhibition of E2-conjugating enzymes; the D88A mutation abolishes this activity [27, 29]. Introducing OTUB1-D88A into HGC-27-Vector/CST1 cells decreased GPX4 stability compared with OTUB1-WT, with a more pronounced effect in CST1-overexpressing cells (**g**). These results confirm that CST1 stabilizes GPX4 by supporting OTUB1-mediated deubiquitination.

Protein-protein docking predicted a stable CST1–OTUB1–GPX4 complex. 3D structures from SWISS-MODEL and PDB were analyzed using Cluspro (**h**) and PDBePISA, which indicated low binding free energy, suggesting a stable complex (**Figures 4a and b**). LIGPLOT mapping illustrated potential interaction surfaces between CST1, OTUB1, and GPX4 (**Figure 4c**). Truncated CST1 constructs were generated: CST1-FL (aa 1–141), CST1-N (aa 1–73), and CST1-C (aa 74–141) with Myc tags (**I**). Myc-IP in HEK293T cells co-transfected with OTUB1-Flag and GPX4-HA revealed that CST1-FL and CST1-N interact with OTUB1, whereas CST1-FL and CST1-C interact with GPX4 (**J**),

indicating distinct CST1 domains mediate dual binding and stable complex formation.

CST1 reduces intracellular ROS and suppresses ferroptosis via GPX4

Given CST1's role in stabilizing GPX4, a key regulator of ferroptosis, we tested whether CST1 influences ferroptosis. HGC-27-Vector/CST1 cells treated with the ferroptosis inducer erastin (10 μM) maintained higher viability compared with DMSO controls (5A). Conversely, erastin treatment of MKN45-shNC/sh1/sh2-CST1 cells caused a more pronounced viability decrease, which was partially rescued by the ferroptosis inhibitor liproxstatin-1 (1 μM) (5B). These findings suggest that CST1 modulates erastin-induced ferroptosis through GPX4 stabilization.

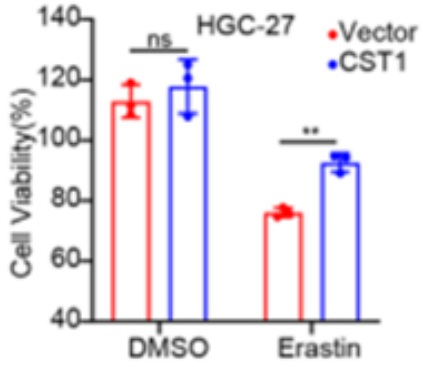

a)

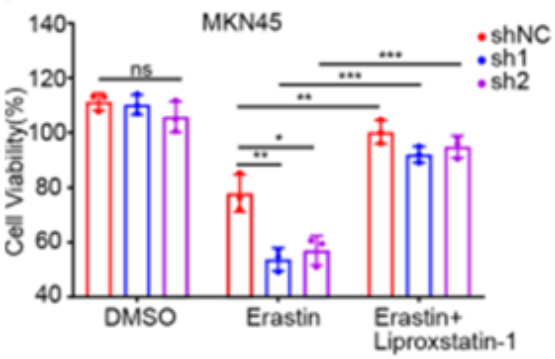

b)

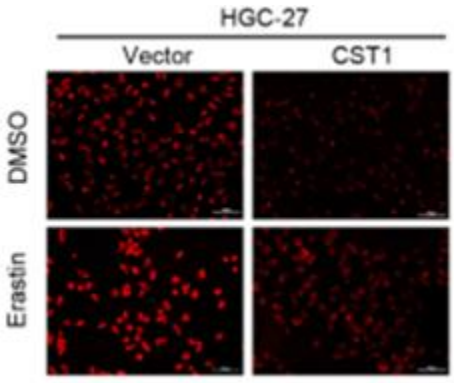

c)

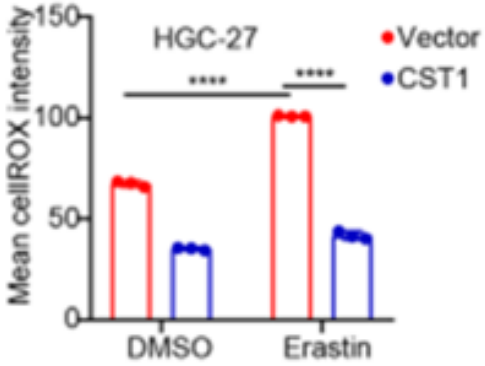

d)

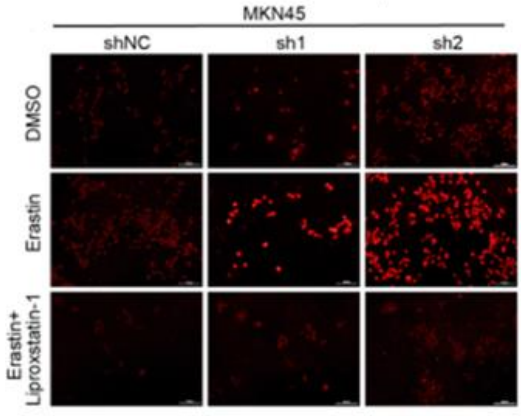

e)

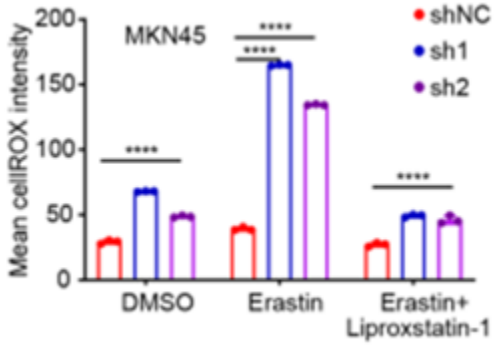

f)

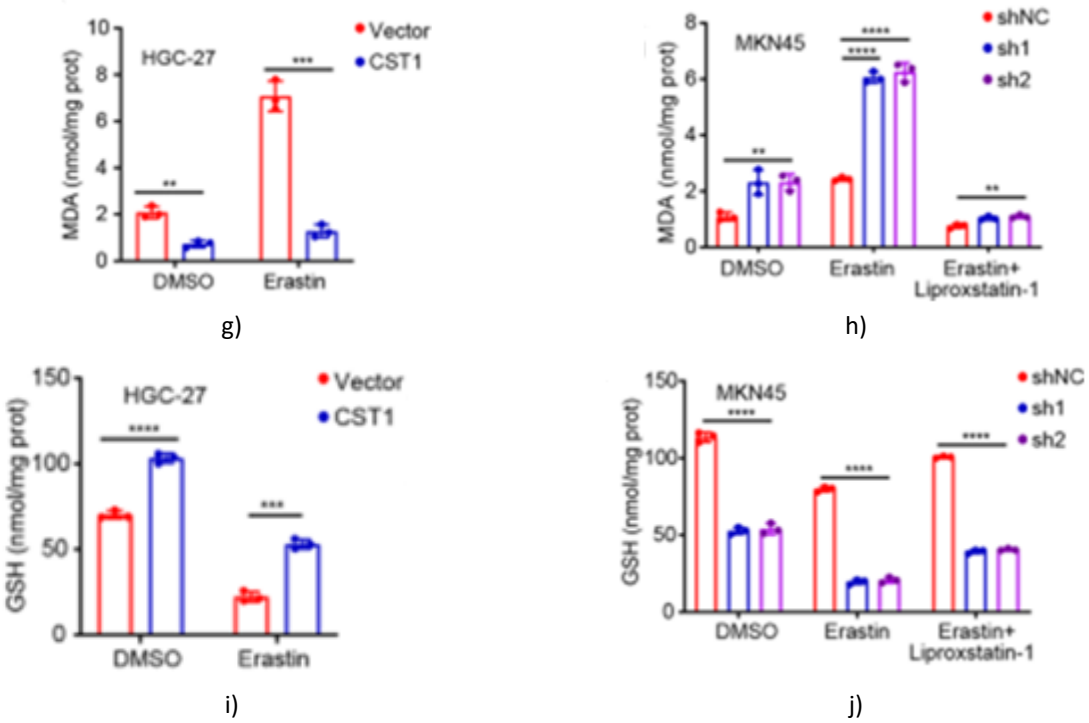

Figure 5. CST1 Attenuates Intracellular ROS Accumulation and Suppresses Ferroptosis via GPX4

a Treatment of HGC-27-Vector and HGC-27-CST1 cells with the ferroptosis inducer erastin (10 μM) resulted in a significantly smaller reduction in cell viability in HGC-27-CST1 cells compared to the DMSO control group (****P < 0.0001). **b** In MKN45-shNC, MKN45-sh1-CST1, and MKN45-sh2-CST1 cells, erastin (10 μM) caused a more pronounced decrease in cell viability relative to the DMSO-treated group (****P < 0.0001). This erastin-induced viability loss in CST1-knockdown cells was partially rescued by co-treatment with the ferroptosis inhibitor liproxstatin-1. **c and d** Fluorescence microscopy revealed that erastin treatment markedly elevated intracellular ROS levels in HGC-27 cells, but this increase was substantially attenuated by CST1 overexpression (****P < 0.0001). **e and f** In contrast, erastin treatment significantly elevated ROS levels in MKN45-sh1-CST1 and MKN45-sh2-CST1 cells compared to the shNC control (****P < 0.0001). This elevation was effectively reversed by liproxstatin-1 treatment. **g** Malondialdehyde (MDA) levels, a marker of lipid peroxidation, were reduced in HGC-27-CST1 cells, with the difference becoming even more pronounced following erastin treatment (****P < 0.0001). **h** Conversely, MDA levels were markedly increased in CST1-knockdown MKN45 cells, particularly after erastin exposure. Treatment with liproxstatin-1 subsequently reduced MDA content in these cells. **i** Glutathione (GSH) levels, a critical substrate for GPX4 activity, were elevated in HGC-27 cells upon CST1 overexpression. **j** In MKN45 cells with CST1 knockdown, GSH levels were significantly reduced, an effect exacerbated by erastin treatment but partially restored by liproxstatin-1 (****P < 0.0001).

Additional fluorescence microscopy analysis of ROS in HGC-27-Vector and HGC-27-CST1 cells confirmed that CST1 overexpression mitigated erastin-induced ROS accumulation (**Figures 5c and d**). Similarly, in MKN45-shNC, sh1-CST1, and sh2-CST1 cells, erastin markedly increased ROS, an effect counteracted by liproxstatin-1 (**Figures 5e and f**).

We further measured GSH and MDA levels. CST1 overexpression in HGC-27 cells lowered MDA content, with greater differences observed post-erastin treatment (**Figure 5g**). In CST1-knockdown MKN45 cells, MDA levels rose significantly, especially after erastin, but decreased upon liproxstatin-1 administration (**Figure 5h**). GSH content increased with CST1 upregulation in HGC-27 cells, whereas it decreased in CST1-downregulated MKN45 cells—an effect amplified by erastin and alleviated by liproxstatin-1 (**Figures 5i and 5j).**

As intracellular iron accumulation is a hallmark of ferroptosis, we assessed iron levels using Prussian blue staining. Neither CST1 overexpression nor knockdown significantly altered intracellular iron content (**Figures 5a and b).**

Collectively, these findings demonstrate that CST1 suppresses intracellular ROS accumulation and thereby inhibits ferroptosis.

CST1 enhances gastric cancer cell migration and invasion via GPX4 in an epithelial-mesenchymal transition-dependent manner

To determine whether GPX4 serves as a functional downstream effector of CST1, we knocked down GPX4 in HGC-27-Vector and HGC-27-CST1 cells using siRNA1 and siRNA2, and confirmed transfection efficiency by Western blot. Conversely, we overexpressed GPX4 in MKN45-shNC, MKN45-sh1-CST1, and MKN45-sh2-CST1 cells, with efficiency validated by Western blot (**Figure 6a**).

Transwell assays were conducted to evaluate the impact of GPX4 on migration and invasion. Compared to HGC-27-CST1 cells, GPX4 knockdown with siRNA1 or siRNA2 markedly impaired migration and invasion capabilities (**Figures 6b and 6d**). In contrast, GPX4 overexpression in MKN45-sh1-CST1 and sh2-CST1 cells significantly enhanced both migration and invasion (**Figures 6b and 6d**). Quantitative analysis of migration and invasion rates in the respective HGC-27 and MKN45 groups corroborated these observations (**Figures 6c and 6e**).

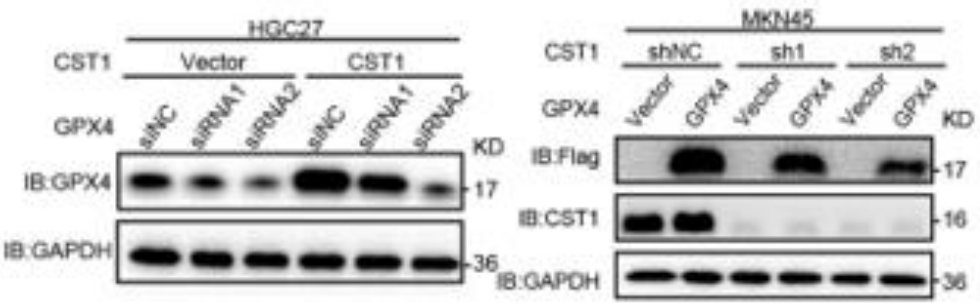

a)

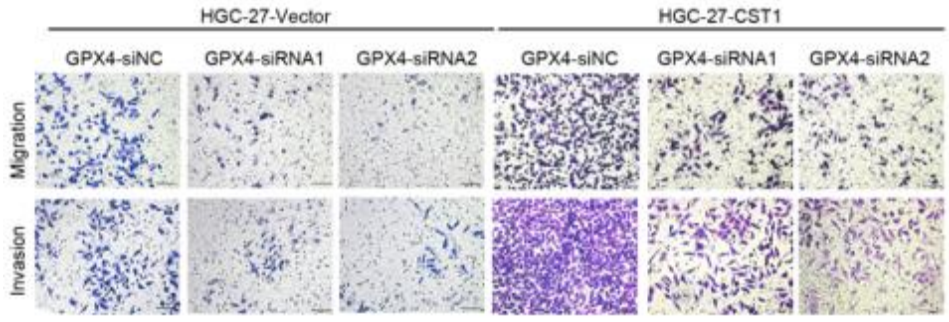

b)

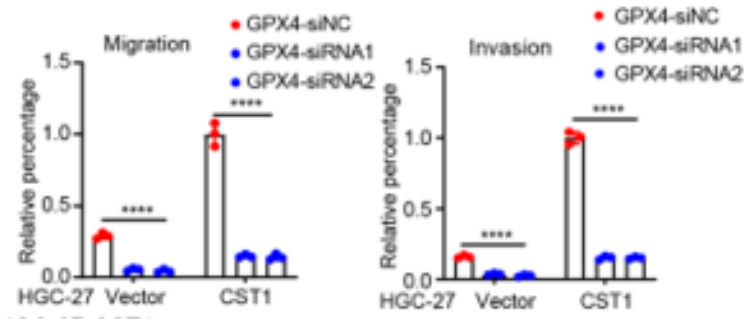

c)

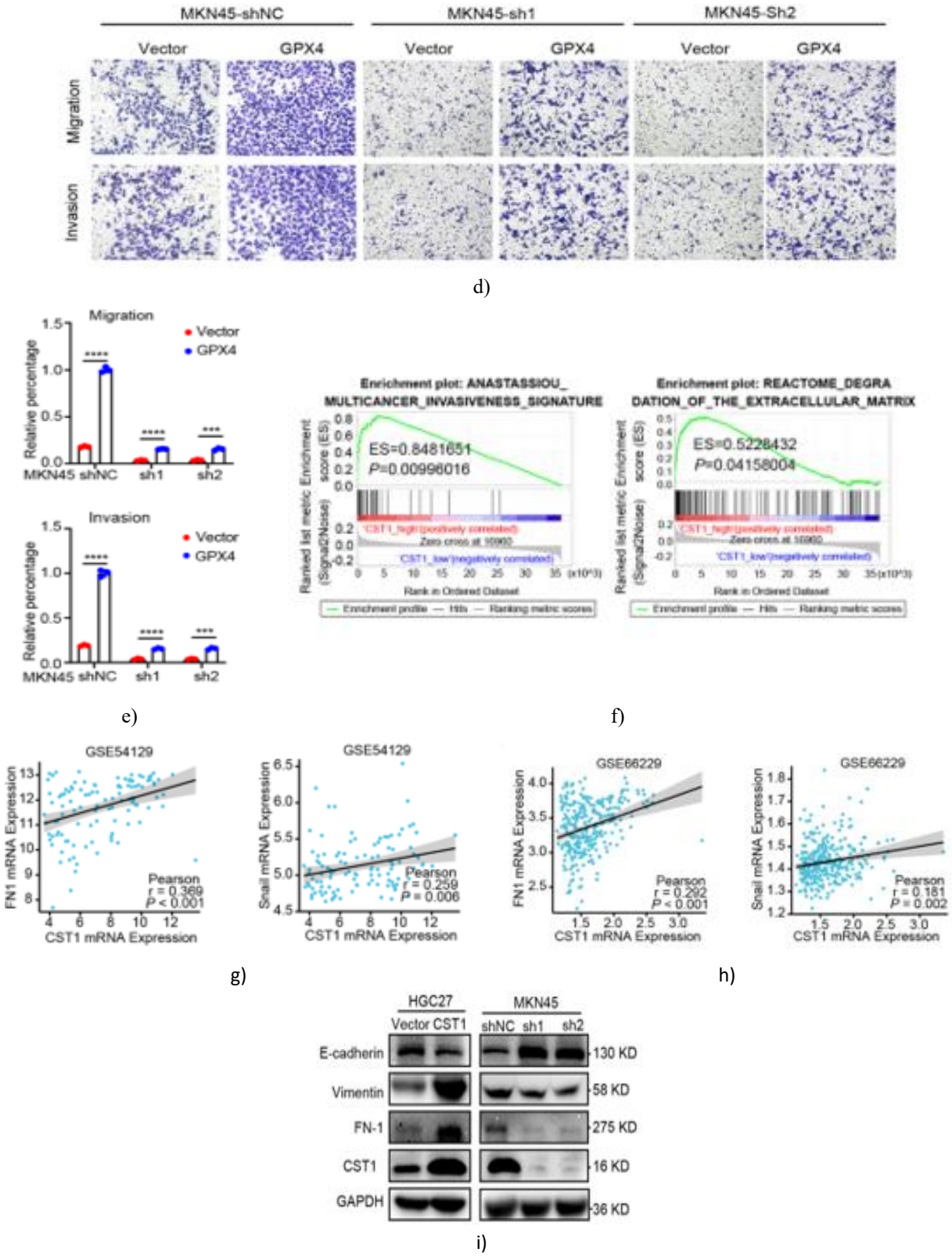

Figure 6. CST1 enhances GPX4 protein stability to drive migration and invasion via epithelial-mesenchymal transition in gastric cancer cells

a Western blot showing GPX4 protein levels in stable HGC-27 and MKN45 cell lines following transient transfection with GPX4-specific siRNAs or plasmids for GPX4 overexpression. **b and c** Transwell migration and invasion assays in HGC-27-Vector and HGC-27-CST1 cells transfected with GPX4 siRNAs or control siRNA. **d and e** Transwell migration and invasion assays in MKN45-shNC, MKN45-sh1-CST1, and MKN45-sh2-CST1 cells following transient GPX4 overexpression or vector control transfection. Data are shown as mean ± SD; statistical analysis was performed using unpaired t-test (****P < 0.0001). **f** Gene set enrichment analysis demonstrating enrichment of gene sets associated with invasiveness and extracellular matrix degradation in samples with high CST1 expression. **g and h** Scatter plots illustrating positive correlations between CST1 and FN1/Snail expression in the GSE54129 and GSE66229 datasets (Pearson's correlation test). **i** Western blot evaluation of E-cadherin, vimentin, and FN1 protein levels in the indicated cell lines.

Epithelial-mesenchymal transition (EMT) plays a critical role in endowing tumor cells with migratory, invasive, and metastatic capabilities [30]. Although CST1 has been reported to facilitate EMT in thyroid and hepatocellular carcinomas [31, 32], its involvement in EMT promotion in gastric cancer remains unexplored. To investigate the pathways through which the CST1-GPX4 axis influences migration and invasion, we conducted RT-qPCR to assess key EMT markers. CST1 overexpression in HGC-27 cells upregulated mRNA levels of mesenchymal markers (N-cadherin and Snail) while downregulating the epithelial marker E-cadherin. Conversely, CST1 knockdown in MKN45 cells reduced mesenchymal marker expression and increased E-cadherin mRNA (**Figure 6a**). These findings suggest a positive association between CST1 and EMT markers.

Gene set enrichment analysis further revealed that pathways linked to invasiveness and extracellular matrix degradation were significantly enriched in tumors with elevated CST1 levels (**Figures**. **6f and 6b**). Analysis of public datasets (GSE54129 and GSE66229) showed strong positive correlations between CST1 expression and that of FN1 (P < 0.001), Snail (P < 0.01), and MMP9 (P < 0.001), whereas no significant correlations were observed with E-cadherin or vimentin (**Figure**. **6g, h, and 6c**). These transcriptomic observations were corroborated at the protein level: CST1 overexpression in HGC-27 cells suppressed E-cadherin while inducing vimentin and FN1 expression, indicative of EMT activation. In contrast, CST1 knockdown in MKN45-sh1/sh2 cells promoted an epithelial phenotype (**Figure 6i**). Collectively, these data establish CST1 as a potent inducer of EMT in gastric cancer cells.

CST1 drives gastric cancer cell migration and invasion by modulating GPX4 Ubiquitination at the K11 Site

To delineate the mechanism by which CST1 regulates GPX4 stability and promotes migration/invasion, we focused on identifying and mutating potential GPX4 ubiquitination sites. Bioinformatics prediction using GPS-Uber and BDM-PUB consistently identified lysine 11 (K11) as a candidate ubiquitination site (**Figure 7a**). We therefore generated a GPX4-K11R mutant. HGC-27-Vector and HGC-27-CST1 cells were co-transfected with wild-type GPX4 (GPX4-WT), the K11R mutant, empty vector, and HA-tagged ubiquitin (Ub-HA). Immunoprecipitation of Myc-tagged GPX4 followed by anti-HA immunoblotting revealed that K11R mutation markedly reduced GPX4 ubiquitination in HGC-27-Vector cells **Figure 7b**, lane 3). This reduction was even more pronounced in CST1-overexpressing cells (**Figure 7b**, lane 6). These results confirm K11 as a bona fide ubiquitination site, although residual ubiquitination suggests additional sites may exist and warrant further investigation.

We next examined the functional consequences of K11 mutation on cell motility. In HGC-27-Vector cells, GPX4-K11R expression enhanced migration and invasion compared to wild-type GPX4. This effect was amplified in HGC-27-CST1 cells, with significantly greater migratory and invasive capacity observed upon K11 mutation (**Figures 7c and d**; statistically significant differences).

CST1 facilitates distant metastasis in Vivo

To assess the in vivo metastatic potential of CST1, we established peritoneal dissemination models in nude mice by intraperitoneal injection of HGC-27-CST1, HGC-27-Vector, or HGC-27 cells with GPX4 knockdown (HGC-27-GPX4#sh). After 60 days, mice bearing CST1-overexpressing cells exhibited a markedly higher number of peritoneal nodules and greater ascites volume compared to controls. Notably, GPX4 knockdown substantially abrogated CST1-driven peritoneal metastasis (**Figure 7a**). Consistent with these findings, CST1-knockdown MKN45 cells produced fewer peritoneal tumors and reduced ascites compared to

control groups (**Figure 7b**). These in vivo data corroborate the pro-metastatic role of the CST1-GPX4 axis in gastric cancer.

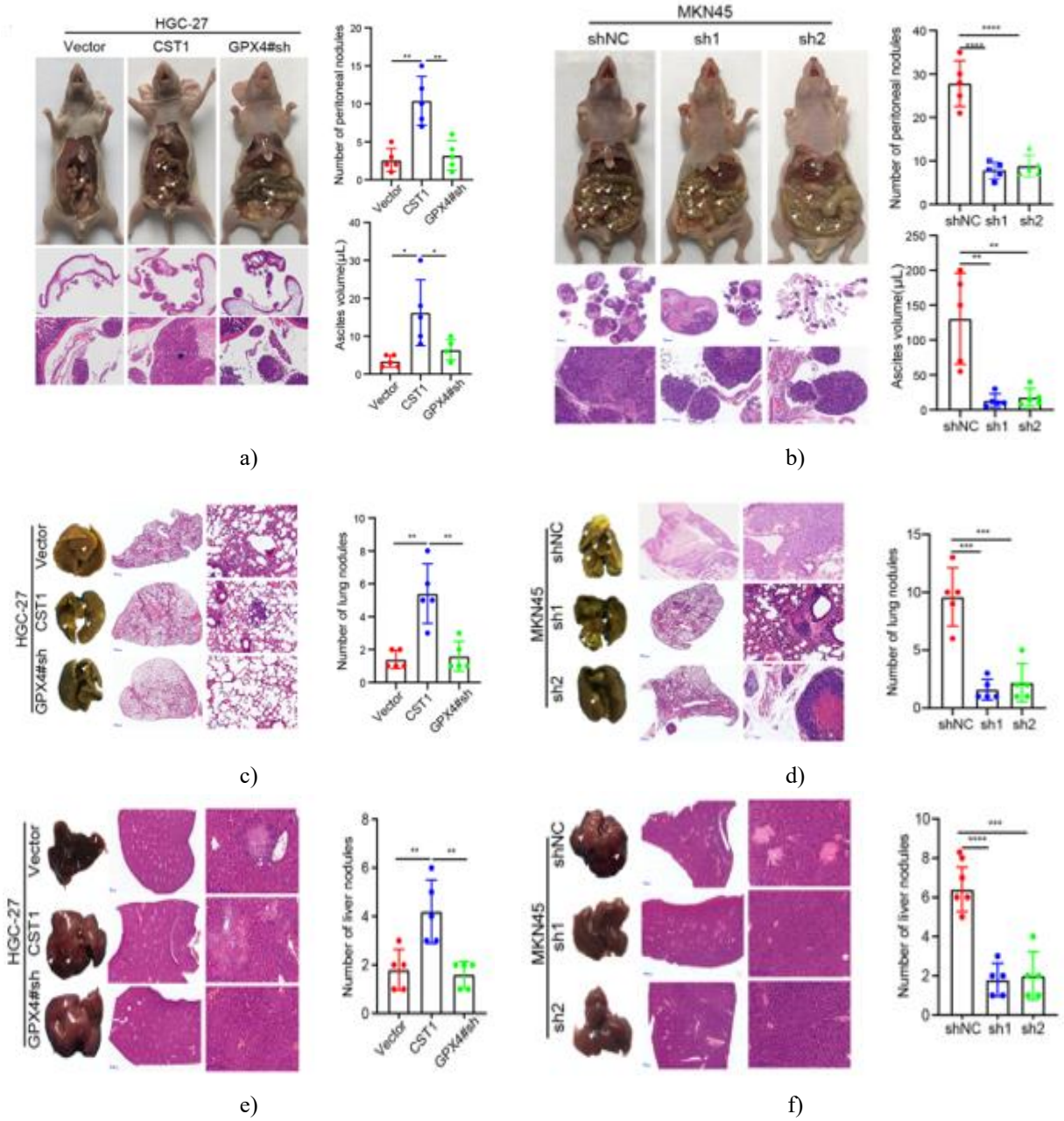

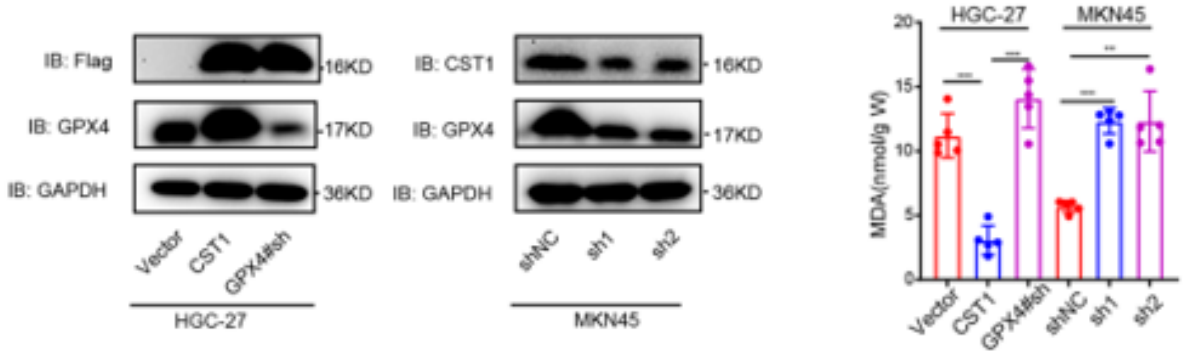

g) h)

Figure 7. CST1 enhances distant metastasis of gastric cancer in vivo.

(**a**) Representative images of peritoneal metastases 60 days after intraperitoneal injection of HGC-27-Vector, HGC-27-CST1, or HGC-27-GPX4#sh cells into nude BALB/c mice. Quantification of tumor nodules and ascites volume is shown on the right; statistical analysis was performed using paired t-test (*p < 0.05, **p < 0.01). (**b**) Peritoneal tumors from CST1-silenced MKN45 xenografts collected 30 days post-injection. Right panel shows the number of nodules and ascites volume with significant reductions in CST1 knockdown groups (**p < 0.01, ****p < 0.0001). (**c**) Lungs from mice 3 months after tail vein injection of HGC-27-Vector, HGC-27-CST1, or HGC-27-GPX4#sh cells. Right panel: enumeration of metastatic nodules revealed significant increases in the CST1-overexpressing group (**p < 0.01). (**d**) Lung metastases observed 8 weeks after tail vein injection of MKN45-shNC/sh1/sh2-CST1 cells. The quantification on the right shows a marked decrease in metastatic nodules upon CST1 silencing (***p < 0.001). (**e, f**) Liver metastasis images collected 2 and 3 months post-tail vein injection of HGC-27-Vector/HGC-27-CST1 and MKN45-shNC/sh1/sh2-CST1 cells. Right panels show statistical analysis of metastatic nodules, demonstrating significant increases with CST1 overexpression (**p < 0.01, ***p < 0.001). (**g**) Western blot analysis of metastatic tumors confirmed CST1 overexpression elevated GPX4 levels, while CST1 knockdown decreased GPX4 expression. (**h**) MDA content in peritoneal metastatic tumor tissues was quantified. CST1 overexpression decreased MDA levels, whereas GPX4 knockdown or CST1 silencing restored or increased MDA levels (***p < 0.001, ****p < 0.0001). Histological sections were visualized at ×0.66 and ×5 magnification.

To investigate the in vivo effect of CST1 on GC metastasis, HGC-27 cells with or without CST1 overexpression, and with GPX4 knockdown, were introduced via lateral tail vein into nude mice. After three months, histological examination showed significantly more metastatic lesions in the lungs and livers of mice injected with CST1-overexpressing cells compared to vector controls. Knockdown of GPX4 mitigated this effect (7C, E). Conversely, CST1-silenced MKN45 cells produced fewer metastatic lesions (7D, F).

Ex vivo analyses demonstrated that CST1 overexpression increased GPX4 levels in metastatic tumor tissues, while CST1 silencing decreased GPX4 expression (7G). Measurement of oxidative stress revealed that CST1 overexpression lowered MDA levels, indicating reduced lipid peroxidation, whereas GPX4 knockdown or CST1 silencing reversed this effect (7H). These findings collectively indicate that CST1 promotes gastric cancer metastasis in vivo, likely through stabilization of GPX4 and inhibition of ferroptosis.

CST1 and GPX4 expression correlate with tumor aggressiveness and poor prognosis in GC patients

To explore the clinical relevance of CST1 and GPX4, their expression was assessed by IHC in 95 GC patient tissue samples. Statistical analysis revealed a strong positive correlation between CST1 and GPX4 expression ($p < 0.0001$) (8A). This correlation was maintained across all differentiation grades of gastric tumors (8B), suggesting that CST1 and GPX4 are co-regulated and may jointly contribute to aggressive GC phenotypes.

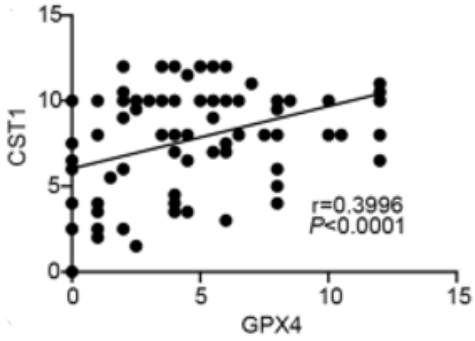
CST1
GPX4
r=0.3996
P<0.0001

a)

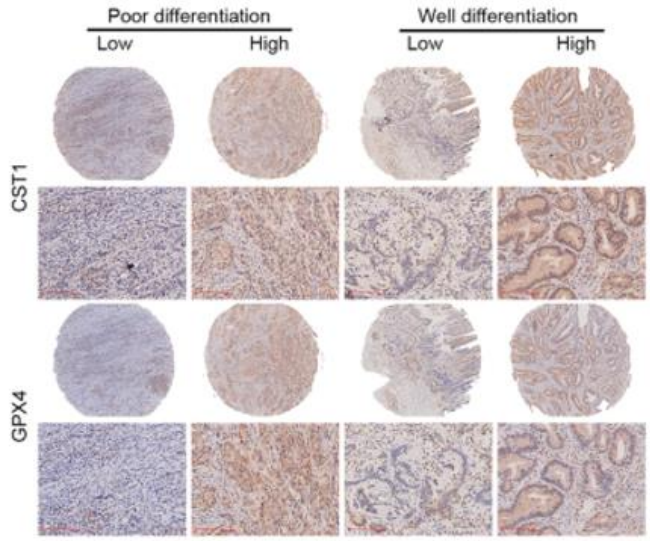
Poor differentiation
Well differentiation
Low
High
Low
High
CST1
GPX4

b)

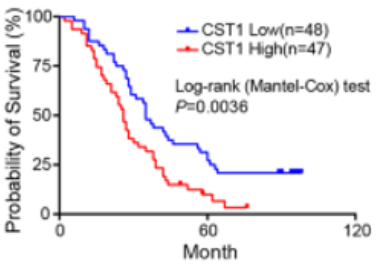
CST1 Low(n=48)
CST1 High(n=47)
Log-rank (Mantel-Cox) test
P=0.0036
Probability of Survival (%)
Month

c)

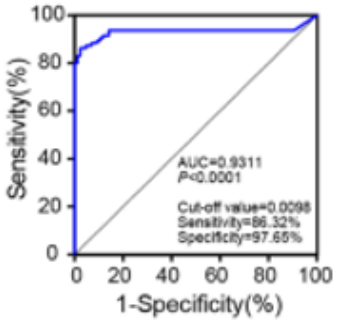
AUC=0.9311
P<0.0001
Cut-off value=0.0098
Sensitivity=86.32%
Specificity=97.65%
Sensitivity(%)
1-Specificity(%)

d)

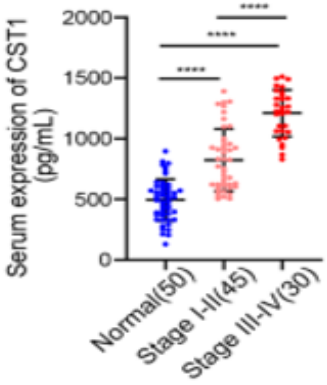
Serum expression of CST1 (pg/mL)
Normal(50)
Stage I-II(45)
Stage III-IV(30)

e)

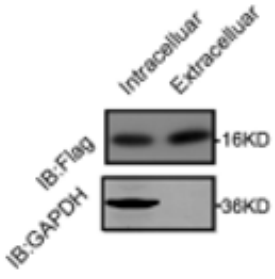
Intracellular
Extracellular
IB:Flag
IB:GAPDH
16KD
36KD

f)

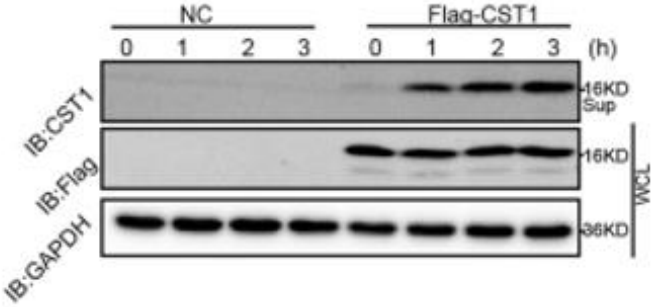
NC
Flag-CST1
0 1 2 3 0 1 2 3 (h)
IB:CST1
IB:Flag
IB:GAPDH
16KD
Sup
16KD
36KD
WCL

g)

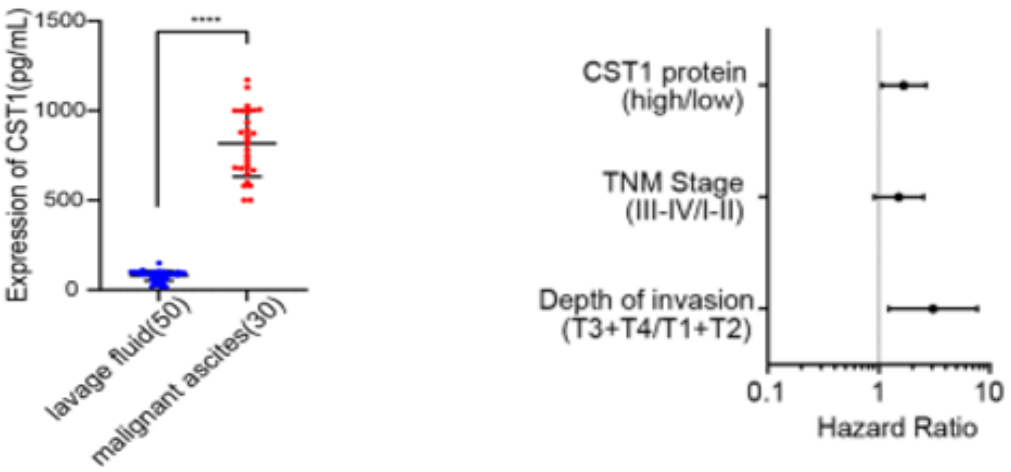

h) i)

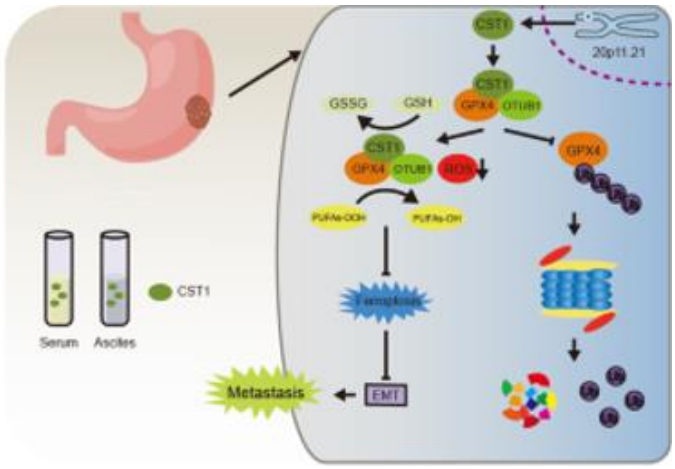

j)

Figure 8. Elevated CST1 and GPX4 levels are linked to aggressive tumor traits and poor outcomes in gastric cancer patients.

(**a**) Immunohistochemical analysis of tissue samples from 95 GC patients revealed a statistically significant positive correlation between CST1 and GPX4 expression using Pearson correlation. (**b**) Representative images showing CST1 and GPX4 protein levels across well-, moderately-, and poorly-differentiated GC tissues. (**c**) Kaplan–Meier survival curves demonstrated that patients exhibiting higher CST1 expression experienced reduced overall survival ($p = 0.0036$). (**d**) Receiver operating characteristic (ROC) curve analysis showed CST1 as a highly sensitive and specific biomarker for GC diagnosis ($AUC = 0.9311$, $p < 0.0001$). (**e**) Serum CST1 levels were quantified by ELISA in 50 healthy individuals, 45 patients with stage I–II GC, and 30 patients with stage III–IV GC. CST1 concentrations were significantly elevated in GC patients relative to healthy controls and increased with advancing tumor stage ($p < 0.0001$). (**f, g**) Western blotting in HEK293T cells transfected with FLAG-CST1 demonstrated the presence of CST1 both intracellularly and in the extracellular medium, with extracellular CST1 accumulation increasing over time. (**h**) ELISA of peritoneal lavage fluid from 50 non-metastatic GC patients and 30 patients with malignant ascites revealed significantly higher CST1 levels in ascitic fluid ($p < 0.0001$). (**I**) Multivariate Cox regression analysis confirmed high CST1 expression as an independent prognostic indicator for poorer outcomes in GC patients. (**j**) Schematic representation illustrating the proposed role of CST1 in promoting GC progression.

Western blot analysis of five paired GC tissues and adjacent normal mucosa confirmed that GPX4 protein was elevated in tumor tissues, consistent with CST1

expression (**Figure**. **1l**). Similarly, GC cell lines (e.g., AGS) expressed higher GPX4 compared with normal gastric epithelial cells (GES-1), paralleling CST1 levels (**Figure**. **2b**).

To examine the CST1-GPX4 correlation in other malignancies, colon cancer tissues and cell lines were analyzed. In five paired colon cancer specimens, CST1 and GPX4 were significantly higher in tumor tissues compared to normal intestinal mucosa (S8C). Colon cancer cell lines (HCT116) also showed elevated CST1 and GPX4, whereas normal epithelial cells (HIEC) exhibited lower expression, with a strong positive correlation between the two proteins (S8D).

Elevated CST1 was associated with poor overall survival ($p = 0.0036$, **Figure 8c**), lower differentiation ($p = 0.027$), and lymph node metastasis ($p = 0.039$). Furthermore, CST1 demonstrated high diagnostic sensitivity and specificity for GC (**Figure 8d**).

Serum ELISA confirmed that CST1 levels were markedly higher in GC patients compared to healthy controls, with levels increasing alongside tumor stage (**Figure 8e**). In HEK293T cells expressing FLAG-CST1, Western blotting revealed both intracellular and extracellular CST1, with extracellular accumulation increasing over time (**Figures 8f and 8g**).

Peritoneal lavage fluid analysis demonstrated significantly elevated CST1 levels in patients with malignant ascites relative to those without metastasis ($p < 0.0001$, **Figure 8h**). Univariate and multivariate Cox regression analyses verified that elevated CST1 independently predicted worse survival outcomes (**Figure 8i**, **Table 3**).

Taken together, these findings indicate that CST1 and GPX4 cooperatively contribute to GC malignancy, and serum CST1 serves as a robust biomarker for diagnosis, prognosis, and metastatic detection.

In this study, we identified CST1 as a critical regulator that promotes metastasis in gastric cancer. Mechanistically, CST1 enhances GPX4 protein stability by recruiting the deubiquitinating enzyme OTUB1, thereby reducing GPX4 ubiquitination. This stabilization decreases intracellular reactive oxygen species (ROS), inhibits ferroptosis, and subsequently facilitates epithelial-mesenchymal transition (EMT) and metastasis of gastric cancer cells (**Figure 8j**).

Previous studies have reported the role of CST1 in cancer metastasis. For example, Cui et al. demonstrated that CST1 promotes hepatocellular carcinoma progression by regulating EMT through the PI3K/AKT pathway [32]. Similarly, Ding *et al*. showed that CST1 enhances invasion, migration, and EMT in papillary thyroid carcinoma [31]. While CST1 has been implicated in gastric cancer progression, the precise mechanisms by which it regulates migration, invasion, and EMT in gastric cancer remain largely unclear.

Here, transcriptome sequencing and bioinformatics analyses revealed that patients with high CST1 expression exhibited poorer prognoses. Functional studies both in vitro and in vivo confirmed that CST1 overexpression promotes gastric cancer cell migration, invasion, and metastasis in nude mice, without significantly affecting cell proliferation.

Through co-immunoprecipitation and mass spectrometry of MKN45 cells, we identified 63 proteins interacting with CST1. KEGG pathway analysis revealed a strong enrichment in ferroptosis-related pathways. Further in vitro validation confirmed that CST1 interacts with GPX4. Functional assays demonstrated that CST1 overexpression reduces erastin-induced ferroptotic cell death, decreases ROS and MDA levels, and increases GSH content. Conversely, CST1 knockdown sensitized cells to ferroptosis, accompanied by elevated ROS and MDA and decreased GSH. These results indicate that CST1 inhibits ferroptosis through GPX4.

Interestingly, CST1 manipulation did not affect GPX4 mRNA levels but significantly altered GPX4 protein levels, suggesting post-translational regulation. GPX4 degradation is known to be mediated via the ubiquitin-proteasome system (UPS) and autophagy. For instance, in A549 lung cancer cells, the deubiquitinase inhibitor PdPT increases GPX4 ubiquitination and promotes protein degradation [33]. To determine the pathway affected by CST1, we treated cells with cycloheximide (CHX), a protein synthesis inhibitor. Overexpression of CST1 reduced GPX4 degradation, indicating that CST1 stabilizes GPX4 via the UPS. Treatment with the proteasome inhibitor MG132 further demonstrated that CST1 reduces GPX4 ubiquitination, supporting a mechanism in which CST1 maintains intracellular ROS homeostasis and protects cells from ferroptosis.

Deubiquitinating enzymes (DUBs) regulate target protein stability by removing ubiquitin chains, thereby controlling protein turnover and cellular functions such as metabolism, differentiation, and proliferation [34, 35]. OTUB1, a member of the DUB family, is broadly expressed in multiple tissues, including kidney, liver, intestine, and brain [36], and plays roles in tumor progression [37]. It has been reported to facilitate EMT

and metastasis in colorectal cancer [38], promote Snail protein stability in esophageal squamous cell carcinoma [39], and modulate PD-L1 stability to influence tumor immunosuppression [29]. In this study, we show for the first time that CST1 recruits OTUB1 to stabilize GPX4 protein, thereby inhibiting ferroptosis and enhancing gastric cancer metastasis.

Moreover, CST1 contributes to EMT in gastric cancer. EMT is influenced not only by genetic and epigenetic changes but also by tumor microenvironmental factors, including cytokines, growth factors, metabolic alterations, and extracellular matrix remodeling. ROS play a dual role during EMT [40]. Moderate ROS levels can drive EMT, whereas excessive ROS can induce cell death [41]. Previous studies indicate that cells in an EMT-like state are more sensitive to ferroptosis inducers [42]. Our findings suggest that CST1 maintains ROS homeostasis through GPX4 stabilization, allowing gastric cancer cells to undergo EMT while avoiding ferroptosis, thereby facilitating metastasis.

Clinically, CST1 expression is elevated in gastric cancer tissues and correlates with poor differentiation and lymph node metastasis. Circulating CST1 levels in patient serum are higher than in healthy controls and correlate with disease progression. ROC curve analysis demonstrated that CST1 improves diagnostic sensitivity and specificity for gastric cancer. Notably, CST1 levels were markedly elevated in peritoneal fluid from patients with metastatic gastric cancer compared with early-stage patients, suggesting a role in peritoneal dissemination and prognostic relevance.

In summary, our findings reveal that CST1 expression increases during gastric cancer metastasis. CST1 recruits OTUB1 to interact with GPX4, reducing its ubiquitination and enhancing protein stability. This process decreases intracellular ROS, inhibits ferroptosis, and promotes EMT and metastasis. Clinically, CST1 detection in blood and peritoneal fluid may provide valuable information for diagnosing gastric cancer, assessing malignancy, and evaluating prognosis.

Materials and Methods

Clinical specimens

Tumor specimens from primary gastric cancer (GC) and paired adjacent non-tumorous gastric tissues were obtained from 185 patients undergoing radical gastrectomy without preoperative neoadjuvant treatment at the First Affiliated Hospital of Soochow University (2009–2019). Complete follow-up information was available for 95 patients, enabling clinicopathological correlation and survival analysis. For transcriptome profiling, eight paired samples were selected: four from patients without metastasis and four from those with peritoneal dissemination; sequencing was outsourced to OE Biotech (Shanghai, China). Other specimens were snap-frozen at −80°C for subsequent RT-qPCR or formalin-fixed and paraffin-embedded for immunohistochemical staining. Additionally, serum, malignant ascitic fluid, and peritoneal lavage samples were harvested from GC patients and healthy controls for enzyme-linked immunosorbent assay (ELISA).

Informed consent was obtained from all participants in writing. The research protocol adhered fully to the Declaration of Helsinki and received approval from the Institutional Ethics Committee of the First Affiliated Hospital of Soochow University (approval reference: 2020381).

Cell lines and maintenance

The gastric cancer cell lines AGS, HGC-27, MKN45, and SNU-1 were acquired from Procell Life Science & Technology Co., Ltd. (Wuhan, China), while MGC803 was sourced from Beyotime Biotechnology (Shanghai, China). The laboratory of Dr. Zhou maintained stocks of HEK293T cells, the normal gastric epithelial line GES-1, additional GC lines (BGC-823 and SGC7901), colorectal cancer lines (HCT116, HCT-8, SW480, KM12), and the normal intestinal epithelial line HIEC under routine conditions. Recent short tandem repeat (STR) profiling authenticated HGC-27 and MKN45 cells. Mycoplasma testing confirmed all lines were contaminant-free.

Cells were routinely grown in either RPMI 1640 or DMEM base medium containing 10% fetal bovine serum (FBS; Procell, Wuhan, China) and 1% penicillin-streptomycin mixture. Cultures were incubated at 37°C in a humidified environment with 5% CO_2.

Real-Time quantitative PCR (RT-qPCR)

RNA was purified from tissue samples or cultured cells using TRIzol reagent (Invitrogen) following the recommended procedure. RNA quality and concentration were verified spectrophotometrically with a NanoDrop 2000c instrument (Thermo Scientific, Wilmington, USA). Reverse transcription was carried out on 1 μg total RNA using All-In-One 5× RT MasterMix (ABM, Canada). Amplification was performed in an ABI ViiA7 real-time system (Life Technologies, USA) employing

SYBR Green chemistry (ABI). Gene expression levels were determined by the 2^−ΔΔCt method relative to GAPDH housekeeping control.

Immunoblotting (Western Blot)

Whole-cell extracts were prepared using RIPA lysis buffer fortified with protease inhibitors. Protein yields were measured via BCA assay (Beyotime Biotechnology, China). Twenty micrograms of protein per lane were fractionated by sodium dodecyl sulfate-polyacrylamide gel electrophoresis (SDS-PAGE) and transferred to polyvinylidene difluoride (PVDF) membranes. Non-specific binding was blocked with 5% bovine serum albumin in Tris-buffered saline with Tween-20 (TBST) for 1 hour. Primary antibodies were applied overnight at 4°C, followed by three TBST rinses and 1-hour incubation with horseradish peroxidase (HRP)-linked secondary antibodies at room temperature. After final washes, signals were developed using an enhanced chemiluminescent substrate kit (Beyotime Biotechnology, Shanghai, China) and quantified by densitometry in ImageJ.

Antibodies included: GPX4 (rabbit mAb, ab125066, 1:5000; Abcam, Cambridge, MA), OTUB1 (rabbit mAb, ab175200, 1:1000; Abcam), GAPDH (mouse mAb, ab8245, 1:1000; Abcam), CST1 (rabbit pAb, 16025-1-AP, 1:1000; Proteintech, Wuhan, China), Flag-tag (rabbit pAb, 20543-1-AP, 1:1000; Proteintech), c-Myc (rabbit pAb, 10828-1-AP, 1:1000; Proteintech), and HA-tag (rabbit pAb, 51064-2-AP, 1:1000; Proteintech). Secondary HRP-conjugated anti-mouse or anti-rabbit IgG antibodies (1:2000) were supplied by Epizyme Biomedical Technology Co., Ltd (Shanghai, China).

Colony formation assay

To evaluate cell proliferation, a colony formation assay was conducted. In brief, 500 cells were plated into each well of a 6-well plate and cultured for roughly two weeks, allowing colonies to become visible. The culture medium was refreshed periodically. Once colonies had formed, plates were washed gently and stained with 0.1% crystal violet. Colony numbers were then counted manually.

CCK-8 assay

Cell growth was assessed using the Cell Counting Kit-8 (CCK-8) according to the manufacturer's protocol (Beyotime Biotechnology, Shanghai, China). For this assay, 2000 cells were seeded in 100 µL of culture medium per well in a 96-well plate. Cells were incubated for 24, 48, and 72 hours, respectively. At each time point, 10 µL of CCK-8 reagent was added to each well and incubated for an additional 2 hours at 37°C. The absorbance at 450 nm, which reflects cell viability, was measured using a microplate reader.

Migration and invasion assays

Cell migration was examined with a wound-healing assay. Cells in the logarithmic growth phase were seeded into 6-well plates. When cells reached approximately 90% confluency, a straight reference line was drawn on the bottom of the plate, and three perpendicular scratches were made using a sterile 100 µL pipette tip. Detached cells were removed by gently washing with PBS twice. Images of the scratch area were captured at 0 and 24 hours under an inverted microscope at ×10 magnification to assess migration.

For invasion analysis, transwell assays were performed using 24-well chambers with 8.0 µm pore-size inserts coated with Matrigel (BD Biosciences, Cat# 356234). GC cells were trypsinized, resuspended in serum-free RPMI-1640 medium, and 200 µL of cell suspension (5 × 10^5 cells/mL) was added to the upper chamber. The lower chamber contained 600 µL of complete medium with 10% FBS. Cells were incubated for 24, 48, and 72 hours. After incubation, the number of cells that had invaded through the Matrigel was counted in five randomly selected fields per insert at ×400 magnification. All experiments were repeated three times, and mean values were calculated for analysis.

Migration assays

For evaluating cell migration, 5×10^4 gastric cancer cells were plated into transwell chambers with 8.0 µm pores, which were left uncoated with Matrigel. The cells were allowed to migrate for 12 hours before being processed for analysis.

Plasmid, SiRNA, and transfection and lentiviral construction

All siRNAs and plasmids—including Flag-tagged OTUB1, Flag-tagged OTUD5, Myc-tagged CST1, and HA-tagged GPX4—were sourced from Vigene Biosciences (Shandong, China). Plasmid constructs were generated by inserting the corresponding cDNA sequences into the pCMV-MCS vector at AsisI and MluI sites. Mutant constructs, such as OTUB1-D88A and GPX4-K11A, were engineered in-house using the

QuickMutation™ Site-Directed Mutagenesis Kit (Beyotime Biotechnology, Shanghai, China).

Transfections of HEK293T or gastric cancer cells with siRNAs and/or plasmids were performed using Lipofectamine 3000 (Invitrogen, CA, USA), following the manufacturer's recommended procedures. To produce stable cell lines, CST1 overexpression sequences were cloned into the pLenti6.3/IRES/GFP vector containing GFP and puromycin resistance, while CST1 knockdown constructs were packaged into pLKO.1-puro lentiviral vectors. After 72 hours of infection, cells were selected with 10 μg/mL puromycin. GFP expression was monitored via fluorescence microscopy and flow cytometry, and CST1 expression levels were confirmed by RT-qPCR and Western blot.

Immunohistochemistry (IHC)

Sections of 5 μm thickness from paraffin-embedded human or mouse tissues were stained using established IHC protocols. Staining intensity was quantified by taking the median as a threshold: values below the median were categorized as low expression, while those above were considered high expression. Scanned images were analyzed with a NanoZoomer S60 (Hamamatsu Photonics) and ImageJ software.

Co-Immunoprecipitation (Co-IP) and mass spectrometry

Proteins were extracted from tissue samples using an IP buffer containing 50 mM Tris-HCl (pH 7.6), 150 mM NaCl, 5 mM MgCl_2, 10% glycerol, 0.1% NP-40, 0.5 mM DTT, and protease inhibitors. Lysates were incubated with anti-Flag (Sigma-Aldrich) or anti-Myc (Millipore) antibodies for 2 hours at 4°C. Immune complexes were washed five times and subsequently analyzed by LC-MS/MS to identify interacting proteins.

Measurement of intracellular ROS, MDA, and GSH

Intracellular ROS levels were assessed using CellROX™ Deep Red Reagent (Invitrogen) and measured through flow cytometry and fluorescence microscopy. Cells were incubated with 5 μM of the reagent for 30 minutes before treatment, and fluorescence was recorded 30 minutes after the treatment. Malondialdehyde (MDA) levels, as a marker of lipid peroxidation, and glutathione (GSH) content, representing cellular antioxidant capacity, were measured using commercial kits (Solarbio Science & Technology Co., Ltd., Beijing, China) according to the manufacturer's instructions. Assays were conducted on both cultured gastric cancer cells and tissue samples from tumors.

In vivo metastasis experiments

Male BALB/c nude mice aged 4–5 weeks were purchased from Shanghai SLAC Laboratory Animal Co., Ltd. Mice were maintained under specific pathogen-free conditions with a constant temperature of 22 ± 1°C, 50 ± 1% humidity, and a 12-hour light/dark cycle, with unrestricted access to food and water. All procedures, including euthanasia, complied with Soochow University's institutional animal care regulations and adhered to AAALAC and IACUC guidelines (approval number: 202109A0101).

For modeling peritoneal metastasis, HGC-27-Vector or HGC-27-CST1 cells (1 × 10^7) suspended in 200 μL of PBS mixed with Matrigel were injected into the peritoneal cavity of mice and maintained for 60 days (n = 5 per group). Similarly, MKN45-shNC, MKN45-sh1-CST1, or MKN45-sh2-CST1 cells (5 × 10^6) were administered intraperitoneally for 30 days (n = 5 per group). After euthanasia, the number of peritoneal metastatic nodules was quantified, and tissues were collected for hematoxylin and eosin (HE) staining.

To establish lung and liver metastasis models, 5 × 10^6 gastric cancer cells were injected into the tail vein in 100 μL of sterile PBS. Mice were euthanized at day 60 (MKN45 cell lines) or day 90 (HGC-27 cell lines), and metastatic lesions in the lungs and livers were examined. Lungs were fixed in Bouin's solution (G-CLONE, Beijing, China), while livers were fixed in 4% paraformaldehyde, embedded, and stained with HE for histopathological analysis.

Bioinformatic analyses

Computational analyses were performed using R, command-line tools, and online bioinformatics platforms. Public databases such as TCGA (https://gdac.broadinstitute.org/), GEO (https://www.ncbi.nlm.nih.gov/geo/), and Kaplan-Meier Plotter (http://kmplot.com/analysis/) were used for transcriptomic and survival analyses. Protein-protein interaction predictions were carried out using BioGRID (http://thebiogrid.org/) and IntAct (https://www.ebi.ac.uk/intact/home).

Protein docking studies

To model potential interactions between CST1, OTUB1, and GPX4, three-dimensional protein structures were

obtained from SWISS-MODEL and the PDB database. Docking predictions were performed with ClusPro (https://cluspro.bu.edu/), followed by interface analysis using PDBePISA (https://www.ebi.ac.uk/msd-srv/prot_int/pistart.html). Conformational mapping and visualization of docking interfaces were performed with PyMOL (https://pymol.org/) and LIGPLOT (https://www.ebi.ac.uk/thornton-srv/software/LigPlus/).

Statistical methods

All data analyses were conducted using SPSS 26.0 (IBM Corp.) and GraphPad Prism 9. Continuous variables are presented as mean ± standard deviation (SD). Comparisons between groups were performed using one-way ANOVA or Student's t-test, while categorical variables were compared using Pearson's χ^2 test. Kaplan-Meier survival curves were generated and compared using the log-rank test. A p-value of < 0.05 was considered statistically significant.

Acknowledgments: This study was supported by grants from the National Natural Science Foundation of China (NSFC, nos. 81902969, 81902977, 81871952). Jiangsu Provincial Key Research and Development Program, China (no. BE2020657). Gusu Health Talents Cultivation Program, China (no. GSWS2019008). Gusu Leading Talent Program for Innovation and Entrepreneurship (no. ZXL2021441). Postgraduate Research & Practice Innovation Program of Jiangsu Province (no. KYCX22_3218). We thank MedSci Corporation (Shanghai, China) for language editing of this article. In addition, We thank Prof. Changshun Shao and Prof. Yufang Shi, Soochow University Institutes for Translational Medicine, for their helpful discussion of our work and manuscript preparation.

Conflict of Interest: None

Financial Support: None

Ethics Statement: None

References

1. Sung H, Ferlay J, Siegel RL, Laversanne M, Soerjomataram I, Jemal A, et al. Global cancer statistics 2020: GLOBOCAN estimates of incidence and mortality worldwide for 36 cancers in 185 countries. CA Cancer J Clin. 2021;71:209–49.
2. Smyth EC, Moehler M. Late-line treatment in metastatic gastric cancer: today and tomorrow. Ther Adv Med Oncol. 2019;11:1758835919867522.
3. Abrahamson M, Alvarez-Fernandez M, Nathanson CM. Cystatins. Biochem Soc Symp. 2003;70:179–99.
4. de Sousa-Pereira P, Amado F, Abrantes J, Ferreira R, Esteves PJ, Vitorino R. An evolutionary perspective of mammal salivary peptide families: cystatins, histatins, statherin and PRPs. Arch Oral Biol. 2013;58:451–8.
5. Hiltke TR, Lee TC, Bobek LA. Structure/function analysis of human cystatin SN and comparison of the cysteine proteinase inhibitory profiles of human cystatins C and SN. J Dent Res. 1999;78:1401–9.
6. Tseng CC, Tseng CP, Levine MJ, Bobek LA. Differential effect toward inhibition of papain and cathepsin C by recombinant human salivary cystatin SN and its variants produced by a baculovirus system. Arch Biochem Biophys. 2000;380:133–40.
7. Liu Y, Yao J. Research progress of cystatin SN in cancer. Onco Targets Ther. 2019;12:3411–9.
8. Liu Y, Ma H, Wang Y, Du X, Yao J. Cystatin SN affects cell proliferation by regulating the ERalpha/PI3K/AKT/ERalpha loopback pathway in breast cancer. Onco Targets Ther. 2019;12:11359–69.
9. Jiang J, Liu HL, Tao L, Lin XY, Yang YD, Tan SW, et al. Let7d inhibits colorectal cancer cell proliferation through the CST1/p65 pathway. Int J Oncol. 2018;53:781–90.
10. Dai DN, Li Y, Chen B, Du Y, Li SB, Lu SX, et al. Elevated expression of CST1 promotes breast cancer progression and predicts a poor prognosis. J Mol Med. 2017;95:873–86.
11. Kim JT, Lee SJ, Kang MA, Park JE, Kim BY, Yoon DY, et al. Cystatin SN neutralizes the inhibitory effect of cystatin C on cathepsin B activity. Cell Death Dis. 2013;4:e974.
12. Oh BM, Lee SJ, Cho HJ, Park YS, Kim JT, Yoon SR, et al. Cystatin SN inhibits auranofin-induced cell death by autophagic induction and ROS regulation via glutathione reductase activity in colorectal cancer. Cell Death Dis. 2017;8:e2682.
13. Choi EH, Kim J-T, Kim JH, Kim S-Y, Song EY, Kim JW, et al. Upregulation of the cysteine protease inhibitor, cystatin SN, contributes to cell proliferation and cathepsin inhibition in gastric cancer. Clin Chim Acta. 2009;406:45–51.

14. Kim J, Bae DH, Kim JH, Song KS, Kim YS, Kim SY. HOXC10 overexpression promotes cell proliferation and migration in gastric cancer. Oncol Rep. 2019;42:202–12.
15. Chen S, Liu Y, Zhang K, Chen L. CST1 promoted gastric cancer migration and invasion through activating Wnt pathway. Cancer Manag Res. 2021;13:1901–7.
16. Tang D, Chen X, Kang R, Kroemer G. Ferroptosis: molecular mechanisms and health implications. Cell Res. 2021;31:107–25.
17. Jiang X, Stockwell BR, Conrad M. Ferroptosis: mechanisms, biology and role in disease. Nat Rev Mol Cell Biol. 2021;22:266–82.
18. Ubellacker JM, Tasdogan A, Ramesh V, Shen B, Mitchell EC, Martin-Sandoval MS, et al. Lymph protects metastasizing melanoma cells from ferroptosis. Nature. 2020;585:113–8.
19. Nagpal A, Redvers RP, Ling X, Ayton S, Fuentes M, Tavancheh E, et al. Neoadjuvant neratinib promotes ferroptosis and inhibits brain metastasis in a novel syngeneic model of spontaneous HER2+ve breast cancer metastasis. Breast Cancer Res. 2019;21:94.
20. Forcina GC, Dixon SJ. GPX4 at the crossroads of lipid homeostasis and ferroptosis. Proteomics. 2019;19:e1800311.
21. Pohl SO, Pervaiz S, Dharmarajan A, Agostino M. Gene expression analysis of heat-shock proteins and redox regulators reveals combinatorial prognostic markers in carcinomas of the gastrointestinal tract. Redox Biol. 2019;25:101060.
22. Chen X, Kang R, Kroemer G, Tang D. Broadening horizons: the role of ferroptosis in cancer. Nat Rev Clin Oncol. 2021;18:280–96.
23. Lu Y, Qin H, Jiang B, Lu W, Hao J, Cao W, et al. KLF2 inhibits cancer cell migration and invasion by regulating ferroptosis through GPX4 in clear cell renal cell carcinoma. Cancer Lett. 2021;522:1–13.
24. Park J, Cho J, Song EJ. Ubiquitin-proteasome system (UPS) as a target for anticancer treatment. Arch Pharm Res. 2020;43:1144–61.
25. Pohl C, Dikic I. Cellular quality control by the ubiquitin-proteasome system and autophagy. Science. 2019;366:818–22.
26. Chen X, Yu C, Kang R, Kroemer G, Tang D. Cellular degradation systems in ferroptosis. Cell Death Differ. 2021;28:1135–48.
27. Liu T, Jiang L, Tavana O, Gu W. The deubiquitylase OTUB1 mediates ferroptosis via stabilization of SLC7A11. Cancer Res. 2019;79:1913–24.
28. Ding Y, Chen X, Liu C, Ge W, Wang Q, Hao X, et al. Identification of a small molecule as inducer of ferroptosis and apoptosis through ubiquitination of GPX4 in triple negative breast cancer cells. J Hematol Oncol. 2021;14:19.
29. Zhu D, Xu R, Huang X, Tang Z, Tian Y, Zhang J, et al. Deubiquitinating enzyme OTUB1 promotes cancer cell immunosuppression via preventing ER-associated degradation of immune checkpoint protein PD-L1. Cell Death Differ. 2021;28:1773–89.
30. Bakir B, Chiarella AM, Pitarresi JR, Rustgi AK. EMT, MET, plasticity, and tumor metastasis. Trends Cell Biol. 2020;30:764–76.
31. Ding J, Wang X, Gao J, Song T. Silencing of cystatin SN abrogates cancer progression and stem cell properties in papillary thyroid carcinoma. FEBS Open Bio. 2021;11:2186–97.
32. Cui Y, Sun D, Song R, Zhang S, Liu X, Wang Y, et al. Upregulation of cystatin SN promotes hepatocellular carcinoma progression and predicts a poor prognosis. J Cell Physiol. 2019;234:22623–34.
33. Yang L, Chen X, Yang Q, Chen J, Huang Q, Yao L, et al. Broad spectrum deubiquitinase inhibition induces both apoptosis and ferroptosis in cancer cells. Front Oncol. 2020;10:949.
34. Ernst A, Avvakumov G, Tong J, Fan Y, Zhao Y, Alberts P, et al. A strategy for modulation of enzymes in the ubiquitin system. Science. 2013;339:590–5.
35. D'Arcy P, Wang X, Linder S. Deubiquitinase inhibition as a cancer therapeutic strategy. Pharm Ther. 2015;147:32–54.
36. Nijman SM, Luna-Vargas MP, Velds A, Brummelkamp TR, Dirac AM, Sixma TK, et al. A genomic and functional inventory of deubiquitinating enzymes. Cell. 2005;123:773–86.
37. Saldana M, VanderVorst K, Berg AL, Lee H, Carraway KL. Otubain 1: a non-canonical deubiquitinase with an emerging role in cancer. Endocr Relat Cancer. 2019;26:R1–14.
38. Zhou Y, Wu J, Fu X, Du W, Zhou L, Meng X, et al. OTUB1 promotes metastasis and serves as a marker of poor prognosis in colorectal cancer. Mol Cancer. 2014;13:258.
39. Zhou H, Liu Y, Zhu R, Ding F, Cao X, Lin D, et al. OTUB1 promotes esophageal squamous cell

carcinoma metastasis through modulating Snail stability. Oncogene. 2018;37:3356–68.
40. Hayes JD, Dinkova-Kostova AT, Tew KD. Oxidative stress in cancer. Cancer Cell. 2020;38:167–97.
41. Chatterjee R, Chatterjee J. ROS and oncogenesis with special reference to EMT and stemness. Eur J Cell Biol. 2020;99:151073.
42. Wu J, Minikes AM, Gao M, Bian H, Li Y, Stockwell BR, et al. Intercellular interaction dictates cancer cell ferroptosis via NF2-YAP signalling. Nature. 2019;572:402–6.